Research Experience

Soran Parang

The following report presents a list of selected academic research projects that I have conducted up to now; more details concerning my research experience are accessible through my publications.

• Offset Tracking with Sentinel-1A Ground Range Detected (GRD) products

Estimation of the movement of glacier surfaces and generation of glacier velocity map using patch intensity cross-correlation optimization

• Sentinel-1A TOPS (Terrain Observation with Progressive Scans) Interferometry for measuring the ground displacement field due to the Mw 7.3 earthquake occurred on November 12, 2017, at the Iran-Iraq border (near Ezgeleh), Kermanshah, Iran

• Polarimetric SAR

Generation of covariance and coherency matrices using Quad-Pol products (including HH,VV,HV and VH bands); Speckle Reduction; Decomposition using Freeman-Durden algorithm for determining various scattering mechanisms such as Double-Bounce, Surface and Volume Scattering; Unsupervised Classification using Cloude-Pottier and Wishart algorithms

• InSAR Time Series Analysis using PS (Persistent Scatterers) and SBAS (Small Baseline Subset) approaches for monitoring land subsidence

▫ **SBAS Time Series Analysis for monitoring subsidence in the Mashhad valley, northeastern Iran**:

The SBAS algorithm exploits DS (Distributed Scatterers) and for depletion of the effects of uncompensated geometric decorrelation and temporal decorrelation, differential interferograms characterized by small perpendicular baselines (smaller than the critical ones) and short temporal baselines are utilized. In this study, a stack of 34 unwrapped, co-registered DInSAR interferograms acquired by ENVISAT ASAR sensor (in descending orbit, from Sep. 2003 to Oct. 2008 over the Mashhad valley) was generated. To remove the phase contributions associated with orbital errors, Precise Orbit Ephemerides (POE) produced by the Delft Institute for Earth-Oriented Space Research, and to compensate for the topographic phase, a reference DEM (namely SRTM) have been used. After removing topographic phase contribution, the interferometric phase only contains atmospheric and deformation components. Mitigation of the atmospheric effects is performed at the end of the processing by a filtering operation for extracting the signal with high spatial and low temporal correlation. For each coherent pixel, the time series analysis is performed by Least Squares Adjustment approach with a velocity minimum norm constraint and for connecting independent DInSAR interferograms and coping with the rank deficiency of the design matrix, the Singular Value Decomposition (SVD) is applied.

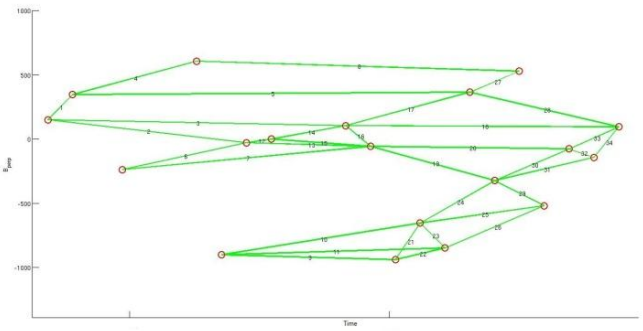

A network of 34 DInSAR Interferograms

Inversion Strategy:

$$L_{ij} = \sum_{r=i}^{j-1} L_r = \sum_{r=i}^{j-1} \Delta t_r \,.\, V_r \qquad A_{ij} = \left[\underbrace{0, \dots, 0}_{i-1}, \underbrace{\Delta t_i, \dots, \Delta t_{j-1}}_{j-i}, \underbrace{0, \dots, 0}_{n-j} \right]$$

$X = \begin{bmatrix} V_1 \\ \vdots \\ V_{n-1} \end{bmatrix}$ n: the number of SAR Scenes $\qquad L = [L_{ij}]_{m\times 1}$ m: the number of suitable DInSAR Interferograms

A: Design Matrix; X: Unknown Vector (Velocities between acquisition dates); L: Observation Vector (from generated Interferograms, deformation in the direction of LOS)

Solution from SVD: V= A†L, In order to diminish some error sources such as atmospheric artifacts, noise and unwrapping errors, a smoothing constraint is added into the inversion problem (Schmidt & Bürgmann, 2003). The Laplacian Smoothing Constraint: $K^2\nabla^2 X=0$, K is the smoothing factor and can be determined by finding the best trade-off point on a curve plotted between RMS (misfit), which is calculated from Least Squares solution, against various related smoothing factors, the optimum smoothing factor will be at the elbow of the curve. Instead of Least Squares Adjustment, WLSA (Weighted Least Squares Adjustment) approach can be used and the weight matrix of the observation defines based on a stack of coherence images.

Pair 5 Pair 11 Pair 13

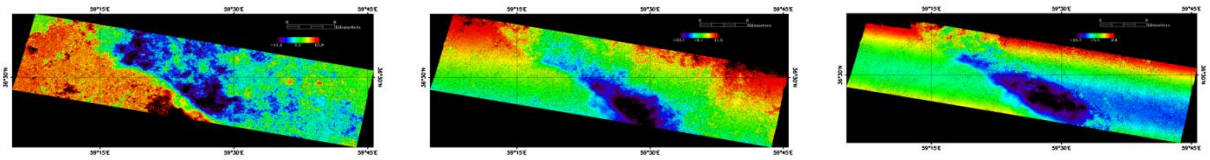

Pair 15 Pair 18 Pair 29

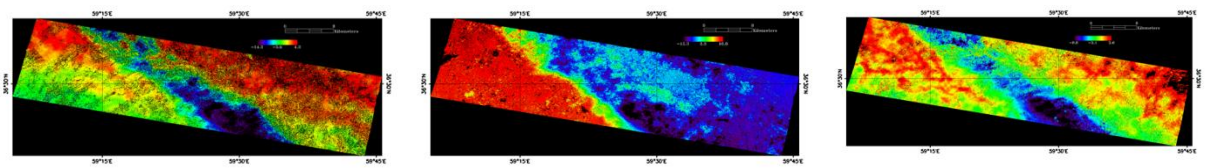

Some unwrapped, geocoded DInSAR Interferograms used in this study (data processing by SNAPHU, DORIS and ENVI)

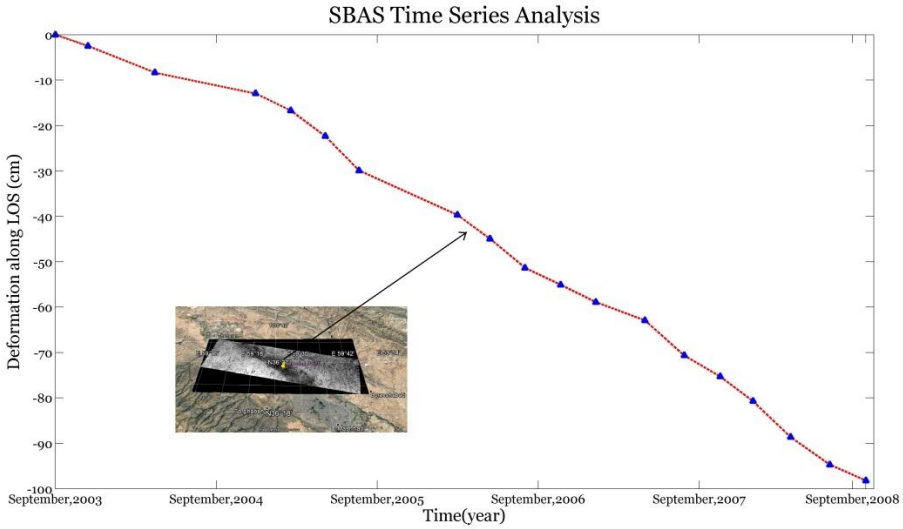

The maximum value of the cumulative subsidence, measured at the selected point, equals ~98 cm during the studied period

• Depth of the Moho Discontinuity from Parker-Oldenburg Inversion and Geopotential Models

The Parker-Oldenburg inversion algorithm is defined as follows:

$$h(x) = F^{-1}\left(-\frac{F[\Delta g(x)]e^{-kz_0}}{2\pi G\rho} - \sum_{n=2}^{\infty}\frac{k^{n-1}}{n!}F[h^n(x)]\right)$$

Where F is the Fourier transform operator; Δg(x) is gravity anomaly; h(x) is the depth to the interface; k is the wavenumber; G is the gravitational constant; ϱ is the density contrast across the interface; and z_0 is the average depth of the horizontal interface. According to this algorithm, the topography of the interface density can be estimated by an iterative inversion procedure. The first approximation of the topography interface is computed by assigning h(x)=0. Iteratively, the value of h(x) is used in the equation to calculate a new estimate of h(x) until a reasonable solution is acquired. Due to the fact that the Parker-Oldenburg inversion method is unstable at high frequencies, a cosine low pass filter is utilized for constraining high frequency signals and series convergence. The high-cut filter (HCF) is defined as follows (WH and SH are the cut-off frequencies):

$$HCF(k) = \frac{1}{2}\left[1 + \cos\left(\frac{k - 2\pi \times WH}{2 \times (SH - WH)}\right)\right] \quad for\ WH < k < SH$$

$$HCF(k) = 0 \quad for\ k > SH$$

$$HCF(k) = 1 \quad for\ k < WH$$

It should be noted that when the difference between two successive approximations is lower than a convergence criterion or when a certain number of iterations is obtained, the iterative procedure will be terminated.

In this study, the complete Bouguer gravity anomaly has been computed from the EGM2008 global geopotential model and ETOPO1 elevation data.

$$\Delta g_{CB} = \Delta g_{FA} - C_{sb} + T.C.$$

Where Δg_{CB} is the complete Bouguer gravity anomaly; Δg_{FA} is the Free-Air gravity anomaly that is calculated from the spherical harmonics of the EGM2008 geopotential model up to degree and order of 2190; C_{sb} is the simple Bouguer reduction that is defined as $C_{sb}=2.\pi.\varrho.G.H^o$ (ϱ: 2670kg/m^3; G: gravitational constant; H^o: orthometric elevation acquired from ETOPO1 model); and T.C. is the terrain effects.

The computed Bouguer anomaly is a combination of long- and short-wavelength features. Generally speaking, a deeper source produces gravity anomalies with longer wavelength than a shallower source with the same size and density. In this study, in order to distinguish between deeper and shallower sources and do away with Bouguer anomalies with short wavelengths associated with shallow crustal sources, the radially averaged power spectrum of the complete Bouguer data has been calculated by Fourier analysis. Considering the log of power of the Bouguer gravity spectrum as a function of wavenumber, the mean depth of the interfaces is estimated by the power spectrum analysis. According to the plot of logarithm of the spectral energy against wavenumber, the spectral energy decays as the wavenumber increases. Mainly, this decay process is controlled by the ensemble average depth of the random distribution of sources, which can be predicted by detecting the linear trends of the plot and fitting a linear function to each segment concerning residual or regional anomalies. The mean depth of the interfaces equals the half of the slope of the segments (Spector & Grant (1970)). The reference level (z_0) for the Parker-Oldenburg inversion approach and cut-off wavelengths for differentiating the regional complete Bouguer anomaly (high wavelength anomalies corresponding to deep sources), which is utilized for the Moho depth estimation, from the residual one (short wavelength anomalies relating to shallow sources) have been derived from the power spectral analysis results. The density contrast between upper mantle and lower crust was computed from CRUST 1.0 and CRUST 2.0 models.

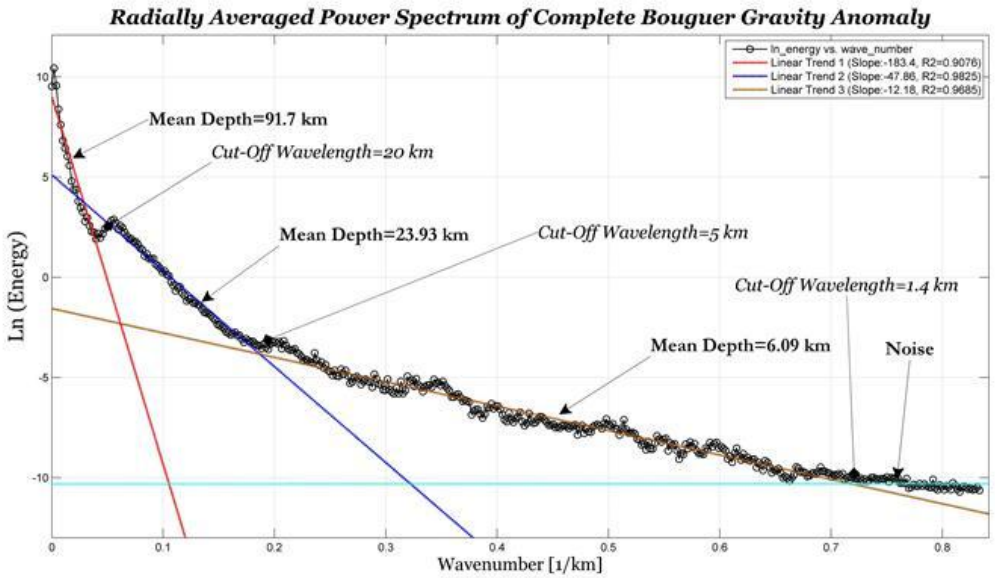

Radially averaged power spectrum of the complete Bouguer anomaly, three linear trends corresponding to causative sources at mean depths of 91.7, 23.93, and 6.09 km

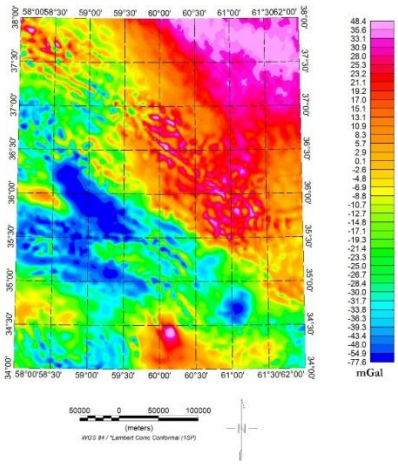

The complete Bouguer anomaly map on the Kopeh Dagh structural zone, northeastern Iran

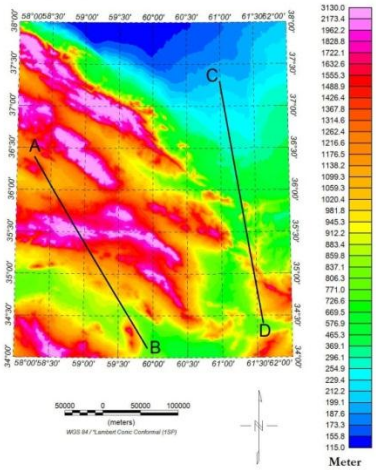

Topography from ETOPO1

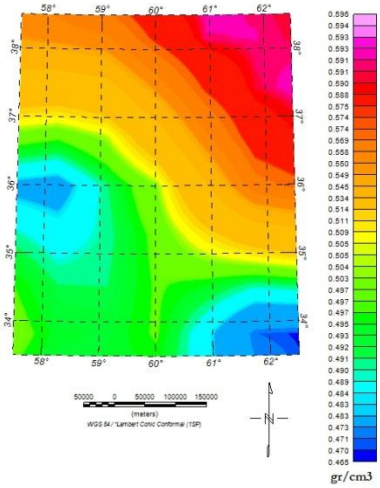

Density contrast between the upper mantle and lower crust calculated from CRUST 1.0 model

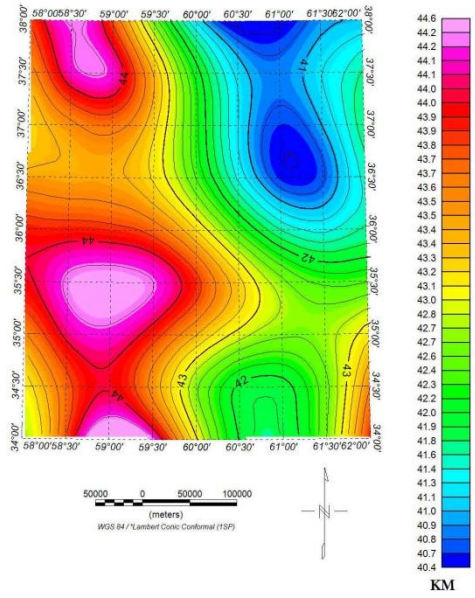

Depth of the Moho discontinuity from the Parker-Oldenburg inversion algorithm

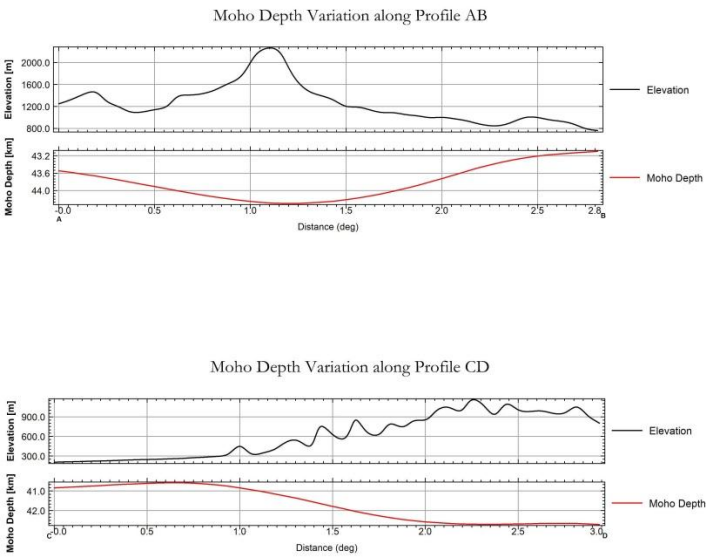

Moho depth variation along profiles AB and CD

• Analytical Modeling of Tsunami Generation Phase in 2010 Chile Earthquake

An earthquake with a magnitude of 8.8 on the moment magnitude scale struck the coastal region of Maule in southwestern Santiago, the capital of Chile, on February 27, 2010. Since the depth of the earthquake has been located at a distance of 35 kilometers of the mean sea-level in Pacific Ocean, the analytical modeling of seafloor deformation for estimating tsunami generation phase and seafloor deformation behavior is of considerable importance. Tsunami waves at the moment of creation in the ocean till their depreciation in coastal regions pass three phases including generation phase, propagation phase, and run-up phase. Tsunami generation phase is created due to the deformation of the seafloor as a result of an earthquake. In other words, the amount of the seafloor deformation after an earthquake can be considered as good criteria for the assessment of the danger of tsunamis. For this aim, according to empirical relationships among earthquake magnitude and factors such as average slip amount D, width W and fault length L, fault's geometrical parameters were determined. In addition, in order to estimate the

displacement field and strain field caused by the earthquake, the Okada analytical model was deployed. Analytical modeling gives the researchers an apt view concerning deformations derived from different kinds of faults. Therefore, the deformation behavior of the Earth's crust resulting from an earthquake, before its occurrence and based upon the kinds of faults in that region, will be predictable. The results of modeling show that the maximum value of displacement along X and Y axes are 0.96 m and 1.6 m respectively and along Z axis, which plays a very important role in raising the sea level, is 4.04 m.

The minimum and maximum values for displacement field and strain field

Parameter	Maximum Value [meter]	Minimum Value [meter]
Ux (displacement field)	0.9567	-3.62
Uy (displacement field)	1.6073	-1.65
Uz (displacement field)	4.048	-0.777
Exx (strain field)	0.00005071	-0.0002136
Eyy (strain field)	0.0000889	-0.0000737
Ezz (strain field)	0.00007025	-0.00004132
Exy (strain field)	0.00009887	-0.0001053
Exz (strain field)	0.000127	-0.0003712
Eyz (strain field)	0.00023614	-0.0002077

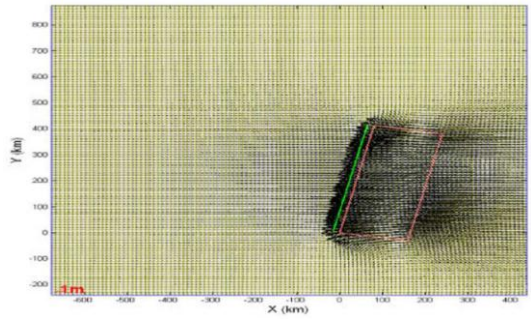

Horizontal displacement field

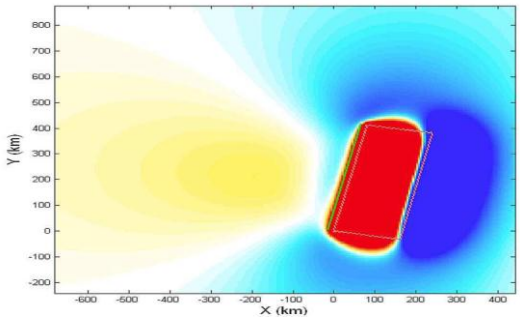

Vertical displacement field

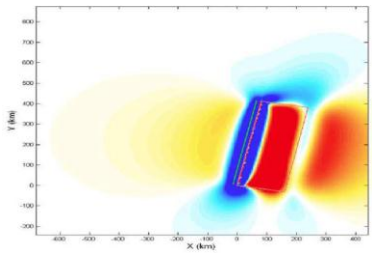
Exx strain component

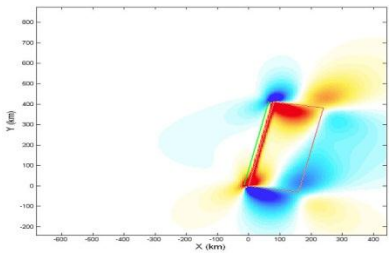
Eyy strain component

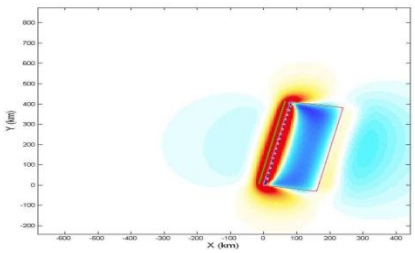
Ezz strain component

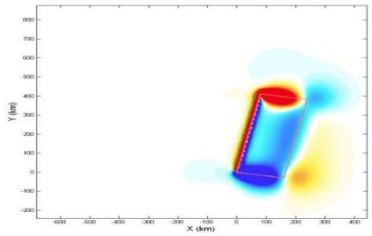
Exy strain component

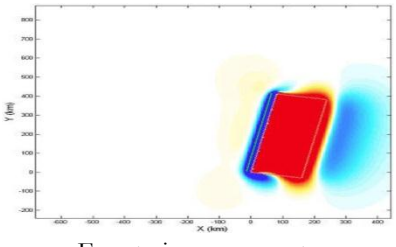
Exz strain component

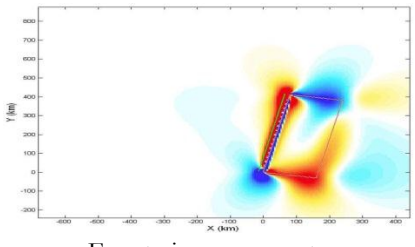
Eyz strain component

• M.Sc. Thesis: Moho Depth Estimation in Iran through Geopotential Models and Euler Deconvolution Method

The Moho discontinuity is the boundary between the Earth's crust and the underlying mantle. The Moho depth in different zones of Iran has been estimated by various approaches like analysis of receiver function method according to teleseismic waves recorded in seismic stations; inversion of terrestrial gravity data and using Bouguer gravity anomaly and free air gravity anomaly; spectral correlation analysis of terrain gravity effects; thermal analysis and using geoid height; Parker-Oldenburg method; Least squares Collection. For instance, the first of crustal thickness variations have been computed from Bouguer anomaly modelling by Dehghani & Makris (1984) for the whole Iran. Based on their results, crustal thickness is 55 km beneath the main Zagros thrust, 45–48 km in eastern Iran and 35 km below the Alborz mountains. In this study, a new approach was used to estimate the Moho depth in structural zones of Iran based on geopotential models and 3D Euler Deconvolution method. The Euler Deconvolution method is a semi-automated process and supports the interpretation of magnetic field data, gravimetry data or gravity gradiometry data. It is used to estimate the location of the source of a magnetic or a gravity field anomaly. Euler Deconvolution method is not dependent on an initial depth or density limitations (Reid et al., 1990; Mushayandebvu et al., 2001). Based on Keating (1998) and Silva & Barbosa (2003), this algorithm is proper to determine depth of vertical and horizontal contacts, so it is good to be used in estimating the crust-mantle boundary (Moho depth).

Thompson (1982) showed that Euler's homogeneity relation could be written in the form:

$$(x - x_0)\frac{\partial T}{\partial x} + (y - y_0)\frac{\partial T}{\partial y} + (z - z_0)\frac{\partial T}{\partial z} = N(B - T)$$

Where (x_0, y_0, z_0) is the position of a source whose total field T, is detected at (x, y, z). The total field has a regional or background value B. N is the degree of homogeneity, interpreted physically as the fall-off rate with distance and geophysically as a Structural Index (SI), Structural Index can change from 0 to 2 for gravity data. Because of high volume of data used in magnetic or gravimetric methods and lack of access to high precision and quality in overall processing of data in whole grid, Euler square window has been defined according to:

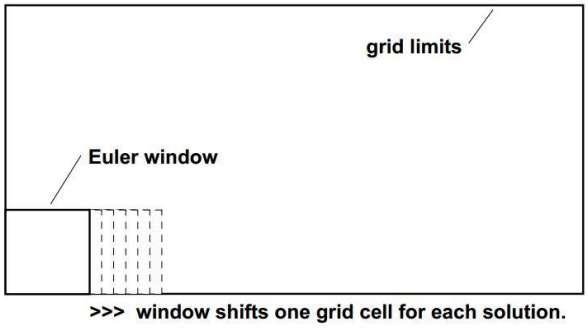

The process is done inside the window and unknown parameters (B, x_0, y_0, z_0) are calculated using least squares adjustment. This window must have two characteristics (Barbosa et al., 1999): 1. It should be large enough to incorporate substantial variation of the field and field gradient.; 2. It should be small enough not to include significant effects from multiple sources.

Mushayandebvu et al. (2004) studied influence of structural index on depth uncertainty and source position using a synthetic anomaly. Their studies show that an estimated depth for an anomaly may considerably change following structural index changes while location (or horizontal) uncertainties (X_{offset},Y_{offset}) won't change much. Although it is possible to have same anomaly using two structural indices, estimating depth of each structural index will be completely different. Another important

parameter is window size which influence estimated depth in each solution. Generally speaking, solutions with much bigger or much smaller depths than window size are not acceptable, in these situations the resulted source cannot fit on geometry of hypothetical model. Reid et al. (1990) studied relation between anomalous depth and window size, they found out that the minimum acceptable depth is equal to window size and its maximum is about three times the window size. Barbosa et al. (2000) showed that it is possible to calculate (x_0, y_0) parameters (horizontal position of source) through selection of proper window size according to the model with no attention to N. But to calculate depth parameter (z_0) which is the most important parameter in interpretation of gravity data, selection of structural index must be done precisely. Window size is a function of model depth and smaller window size provides larger errors for deeper depth because deeper masses have wider anomaly which in order to be included, the window must be wider. In simpler words, small windows deliver proper solutions for shallow anomalies while large windows provide small errors in depth estimation of deep masses.

Geopotential models provide homogeneous and uniformly accurate information on the long wavelengths of the earth's gravity field. Since these Models have long wavelengths of gravity field, they are very suitable in determining Moho depth because short and middle wavelengths are not useful in this case. Accuracy of the geopotential models are usually evaluated by comparing the geoidal heights derived from the models with those of the local GPS-Leveling stations. After comparing EIGEN-GL04C model to GPS-Leveling data, it has been chosen as the most accurate model in Iran. In this research, free air gravity anomaly from EIGEN-GL04C model (Up to degree and order of 360; Long wavelengths of gravity field) as the total field (T) and ETOPO1 Model for considering topography effect were used for estimating Moho depth.

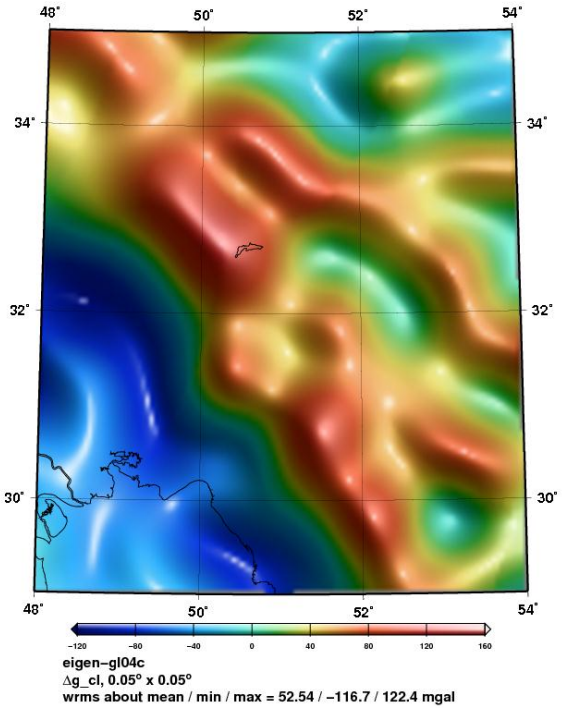

Free air gravity anomaly resulted from EIGEN-GL04C (The Zagros Zone)

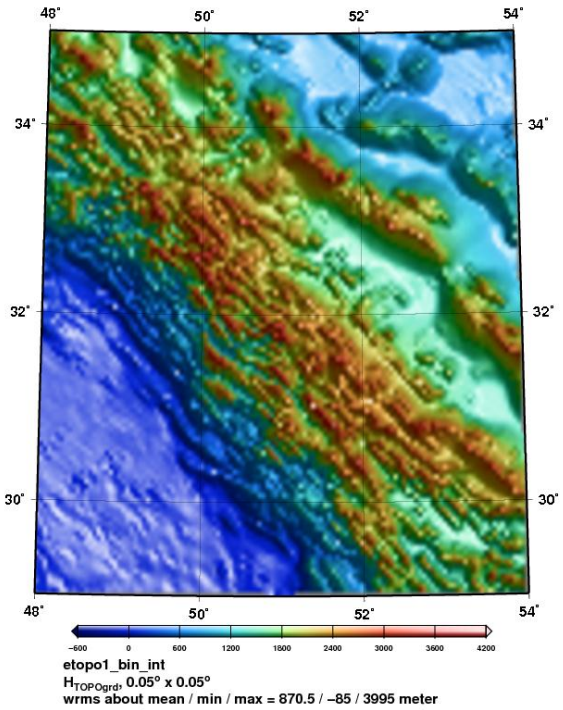

Topography resulted from ETOPO1 (The Zagros Zone)

A lot of research has been done about relationship between anomalous depth and spherical harmonic degree. Bowin (1983) showed that second- and third-degree spherical harmonics are related to sources near to mantle-core boundary. Also Hager (1984) showed that fourth- to ninth-degree spherical harmonics are in relation with density models of subducted slab. Although it is not possible to calculate radial distribution of anomalous masses uniquely, but it is known that deeper and bigger sources produce

lower degree harmonics of gravity field while higher degree harmonics are produced by shallow and smaller sources (Jackson et al., 1991). According to Bowin et al. (1986)studies, maximum depth of sensitivity for each degree of spherical harmonic is defined as $Z_{max}= r_e/(n-1)$; r_e is radius of earth, n is the degree of spherical harmonic and $Z_{max}$is the maximum depth of sensitivity; On the other hand λ (Wavelength)$=2\pi r_e/n$. Since this study aims to find Moho depth (depth of crust-mantle boundary), it can be said the desired depths are below 100 km, so there is a need to use a high pass filter to remove the effect of low frequencies which belong to deep masses, in other words to remove the influence of masses close to the mantle-core boundary and pass high frequencies. In the following figures, free air gravity anomaly and its derivatives in three directions after using a high pass filter with cut-off wavelength of 1000 km are showen. The X and Y derivatives were calculated in the spatial domain using a simple nine-point convolution filter and the Z derivative was computed in the frequency domain using Fast Fourier Transform (FFT).

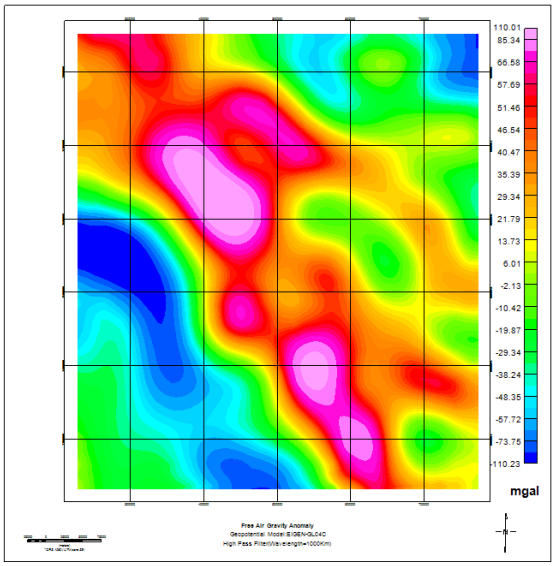

High pass filtered free air gravity anomaly (The Zagros Zone); cut-off wavelength of 1000 km

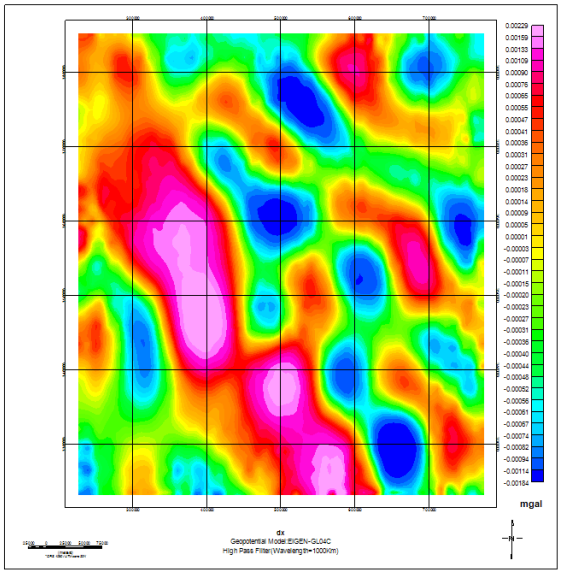

The X derivative

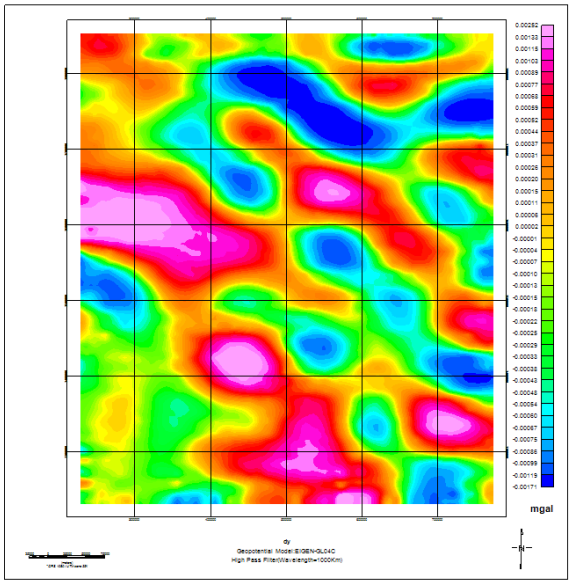

The Y derivative

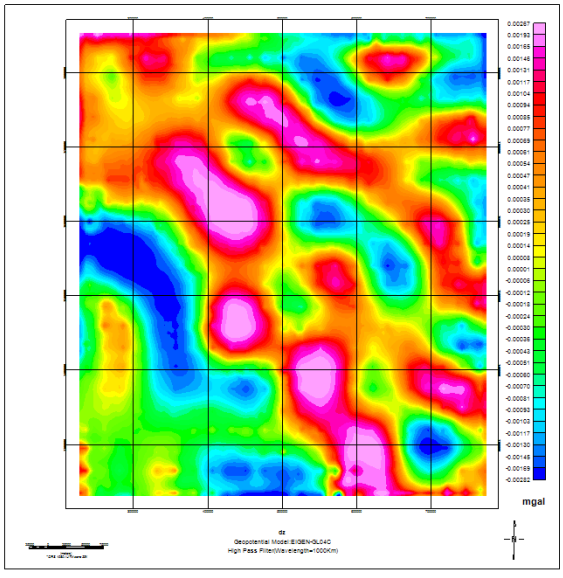

The Z derivative

The Moho depth in the Structural Zones of Iran (Zagros Fold & Thrust Belt, Sanandaj-Sirjan Zone, Alborz, Central Domain, Kopeh Dagh) was estimated by Euler Deconvolution method for 15 km to 55 km window sizes and 0 to 2 structural indices. the best window size and structural index in the structural zones were determined by comparing depths from Euler Deconvolution method and those of seismic studies (receiver function method) in 14 seismic stations of the studied region, then the results were compared to CRUST2.0 model and other research works. In the Zagros zone, the results show that for a window size of 40-45 km and structural index of 0.5 the best Moho depth is estimated using Euler Deconvolution algorithm. The following figure shows the results of estimating Moho depth by Euler Deconvolution method for window sizes of 15 km to 55 km and structural index of 0.5 along AB profile in the Zagros zone. *You can read more*

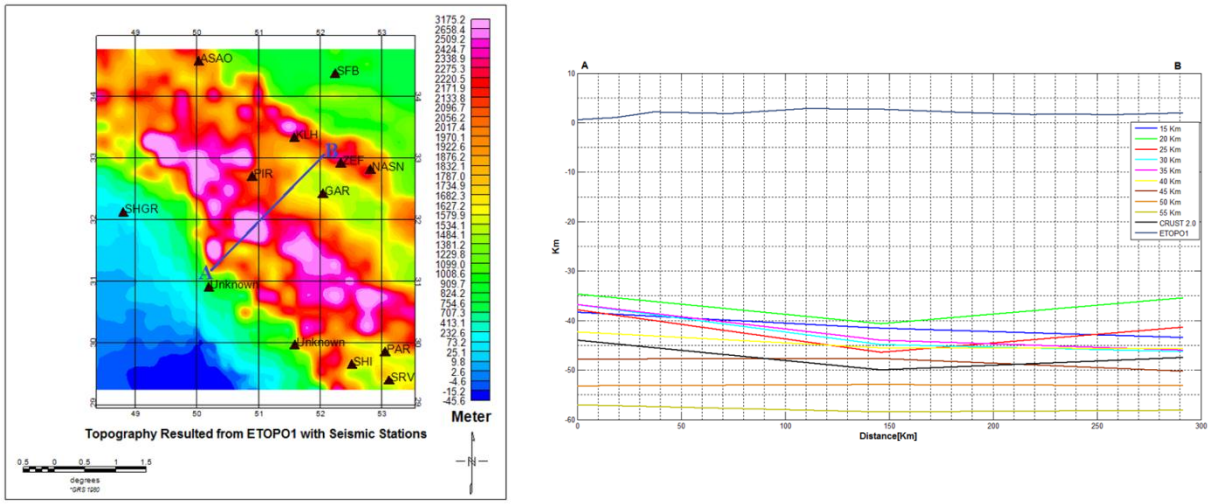

Variation of Moho depth along AB profile in the Zagros Zone

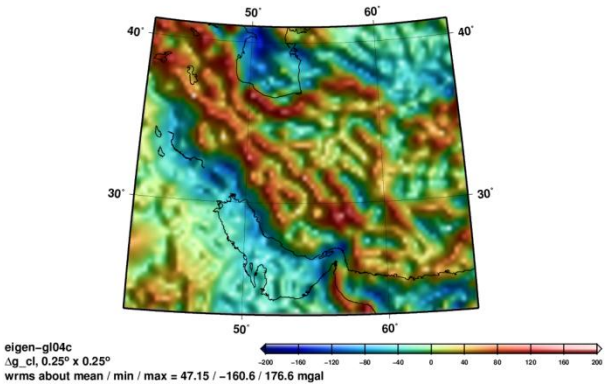

Free air gravity anomaly resulted by EIGEN-GL04C model

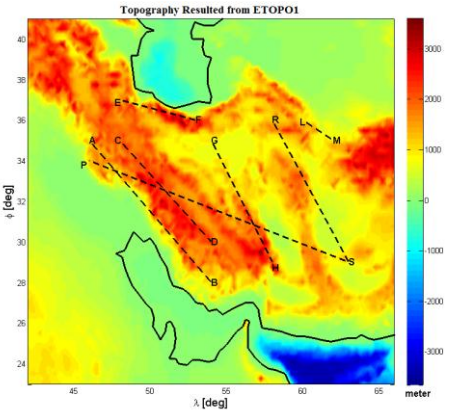

Seven considered profiles in Iran

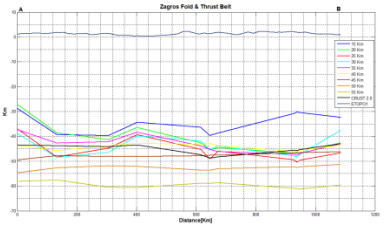

Moho depth variation along AB profile located in the Zagros fold & thrust belt

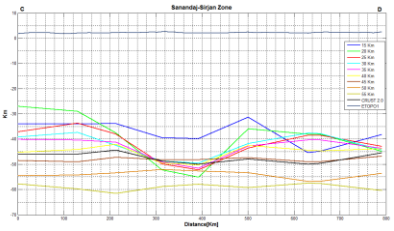

Moho depth variation along CD profile located in the Sanandaj-Sirjan zone

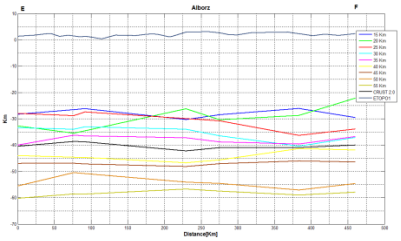

Moho depth variation along EF profile located in the Alborz zone

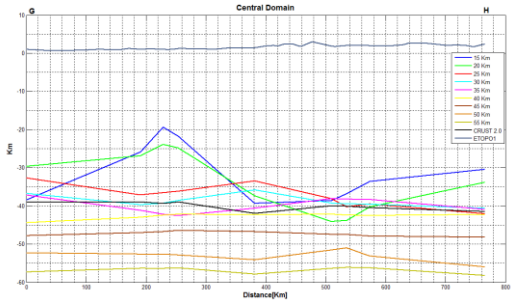

Moho depth variation along GH profile located in the Central domain

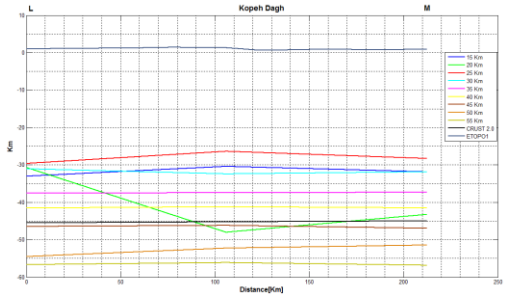

Moho depth variation along LM profile located in the Kopeh Dagh zone

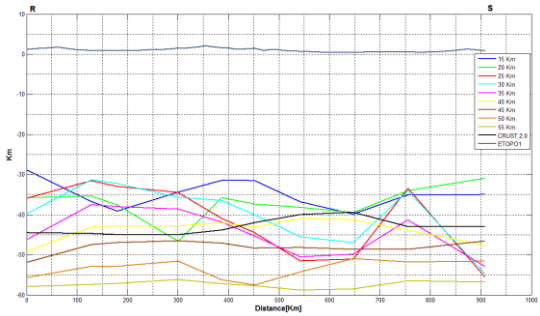

Moho depth variation along RS profile

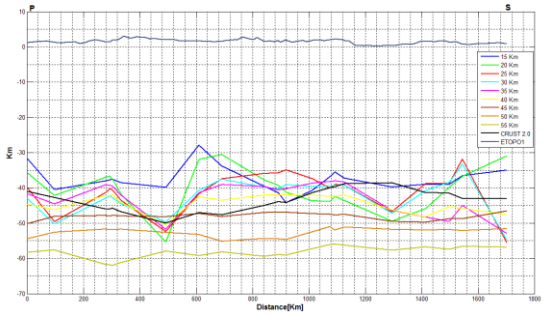

Moho depth variation along PS profile

- **Improving Parallelepiped Classification by Using Elliptical Shape and Combining Minimum Distance in Multispectral Imagery**

Parallelepiped decision is one of the simplest and fastest methods in supervised classification. Although the parallelepiped approach could be implemented easily, it is not capable of separating pixels fallen into overlapping parallelepiped, or fallen outside any parallelepiped. For classifying pixels that are beyond the parallelepiped, we have to expand borders and it will result in emerging inseparable pixels. In this research, we introduce two simple ways to resolve mentioned problems. Firstly, instead of rectangle, we utilize ellipse inscribed in rectangle in order to reduce inseparable pixels. Secondly, we implement minimum distance for inseparable and outside pixels. In order to evaluate the proficiency of this method, the classes derived from it and single minimum distance have been compared to maximum likelihood classifier subsequently. The results demonstrate that this method is more accurate and efficient than simple parallelepiped and single minimum distance.

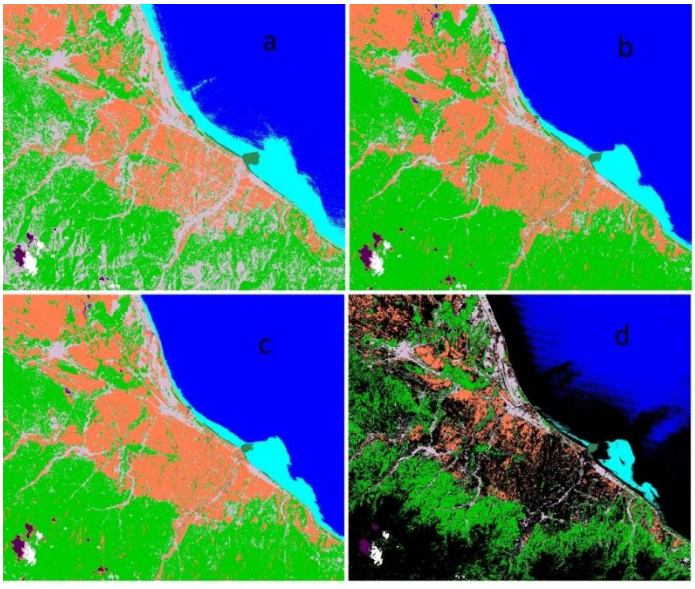

Classified image by: a) maximum likelihood b) minimum distance c) the proposed method d) simple parallelepiped

The evaluation of accuracy

	Overall accuracy	Kappa coefficient
The Proposed Approach	81.6273%	0.7670
Minimum Distance	78.7472%	0.7253
Simple Parallelepiped	45.5455%	0.3869

• Physical Oceanography and Geophysics

▫ Investigation of tsunami formation, Wind waves versus tsunami waves and Tsunami warning system [*Presentation*]

▫ Review of research works done on tsunami hazard evaluation in the Persian Gulf and Caspian Sea

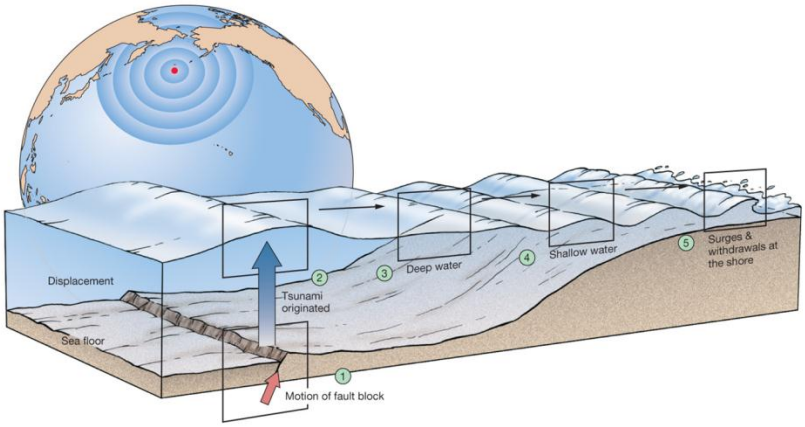

• An Evaluation of Matching Spectral by Using Wavelet Transforms in Hyperspectral Imagery

One of the methods of classification in hyperspectral remotely sensed imagery is using spectral matching. Till this day, many methods including SAM and correlation coefficient are used for matching spectral. Users can obtain features by mentioned methods and laboratory data without any need of field observation. Although above methods are reliable from a mathematical point of view, in presence of aerosols, water vapor and gases in atmosphere, radiance does not interact with reflectance, which is a property of ground feature. In this research, we try to emphasize the generalities and neglect details by dividing radiance and reflectance spectra derived from wavelet transforms into various levels to detect features precisely. Three basis functions, Haar, Doubshi and Meyer have been selected. After classifying the vegetation in the study area using this method, subsequently the resultant class has been compared to another result that is retrieved from SVM method. The results show Haar is more accurate than the others.

Comparison of accuracy

	Haar	Db6	Meyer
Overall accuracy	0.956	0.935	0.914
Kappa coefficient	0.774	0.429	0.090

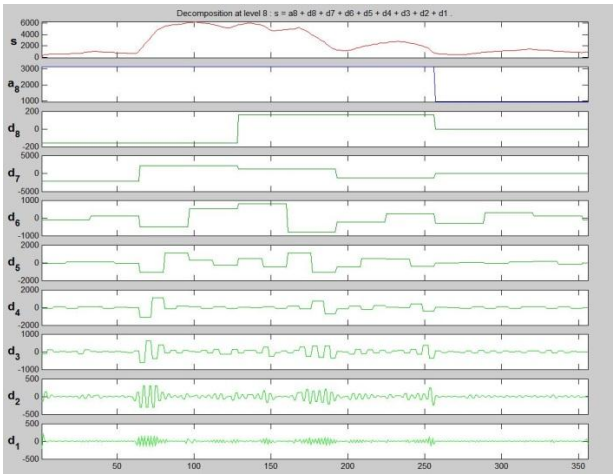

Decomposed reflectance curve of vegetation by Haar basis function

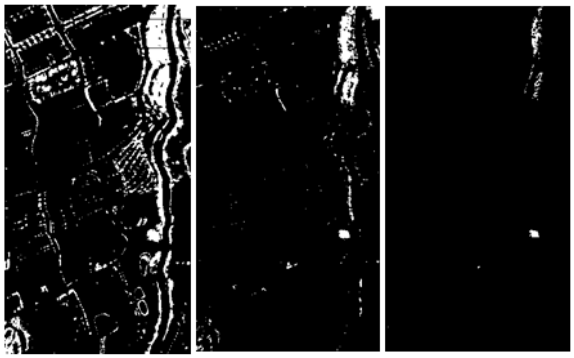

From the left to right, vegetation area calculated by Haar, Db6, Meyer

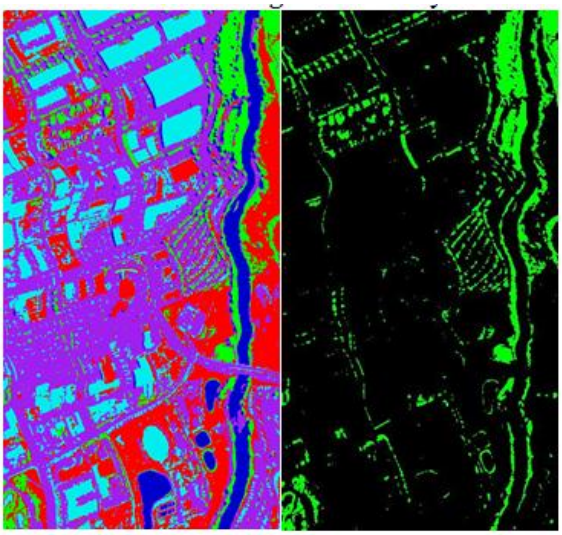

Left: classified image by SVM, Right: vegetation area

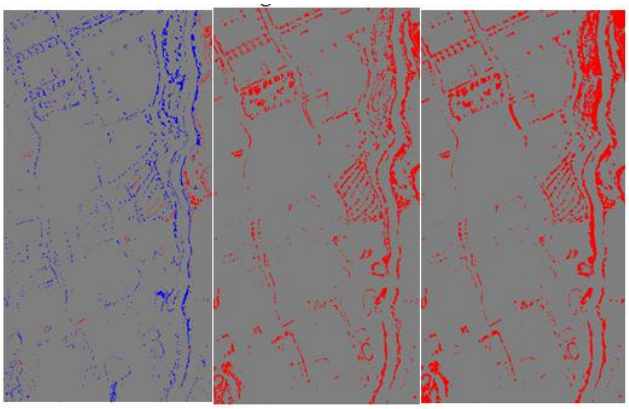

From left to right: the difference between vegetation area calculated by wavelet and SVM, basis functions are: Haar, Db6

• M.Sc. Seminar: Geodynamic studies in Iran using Euler Deconvolution method and gravity gradient tensor

▫ Generating Gravity Gradient Tensor (GGT) in a Geocentric Frame, Local North-Oriented Frame (LNOF) and Orbital Frame (ORF) to degree and order 360 using different Geopotential Models (EIGEN-GL04C, EGM2008)

▫ Using the GGT generated from Geopotential models and GOCE gradiometery data in Euler Deconvolution method and interpreting the obtained results

The Euler Deconvolution algorithm includes the following three equations in which the components of GGT are used.

$$(x - x_0)T_{xx} + (y - y_0)T_{xy} + (z - z_0)T_{xz} = N(B_x - T_x)$$

$$(x - x_0)T_{yx} + (y - y_0)T_{yy} + (z - z_0)T_{yz} = N(B_y - T_y)$$

$$(x - x_0)T_{zx} + (y - y_0)T_{zy} + (z - z_0)T_{zz} = N(B_z - T_z)$$

In above equations, T_x, T_y and T_z are the first-order derivatives of the field at the observation point (x, y, z); T_{xx}, T_{yy}, T_{zz}, T_{xy}, T_{yx}, T_{xz}, T_{zx}, T_{yz} and T_{zy} are the components of the gravitational gradient tensor (second-order derivatives of the field) at the observation point (x, y, z); x_0, y_0 and z_0 are the unknown coordinates of the source; B_x, B_y and B_z are the regional values of the field along the x-, y-, and z-directions; and N is the structural index (SI). SI is the rate at which the field intensity falls off with distance from the source and it depends on the type of source body, which you are looking for, and the type of the potential field data (magnetic or gravity); for gravity data, this factor can range from 0 to 2. To estimate Moho depth using the Euler Deconvolution algorithm, it is assumed that crust-mantle boundary is a horizontal sheet or it has sill-type anomaly, which can be expressed in an infinite 2D space; the best structural index to estimate this anomaly is 0.5. An important parameter in this algorithm is window size that influences the depth of anomaly (z_0) in each solution. The window size should be small enough in order to prevent effects from multiple sources. In addition, it should be large enough to include substantial variations of the field. The unknown parameters (x_0, y_0, z_0, B_x, B_y, B_z) are solved by the least squares estimation in each window. The GGT components can be expressed in terms of spherical harmonic expansion coefficients. In this research, the first-order and second-order derivatives of the disturbing potential (T) in the geocentric Earth-fixed reference frame have been calculated using the formulas presented by Petrovskaya & Vershkov (2010) and geopotential models. In the following figure, the Moho depth in structural zones of Iran, estimated by applying the GGT components calculated from EGM2008 geopotential model in Euler Decovolution algorithm, is shown. The results indicate that the Moho depth is about 49 km beneath the main Zagros thrust, 45-48 km in the Sanandaj-Sirjan zone, 40-42 km in the Kopeh Dagh zone, less than 43 km in the Lut block, about 40 km beneath the Alborz mountains, and 30-36 km in the Makran zone.

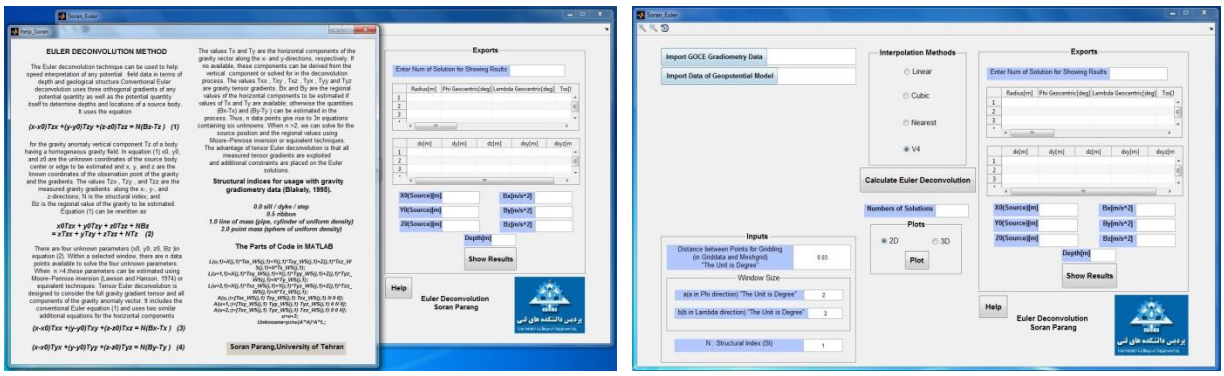

The MATLAB GUI program, which I have written for this project

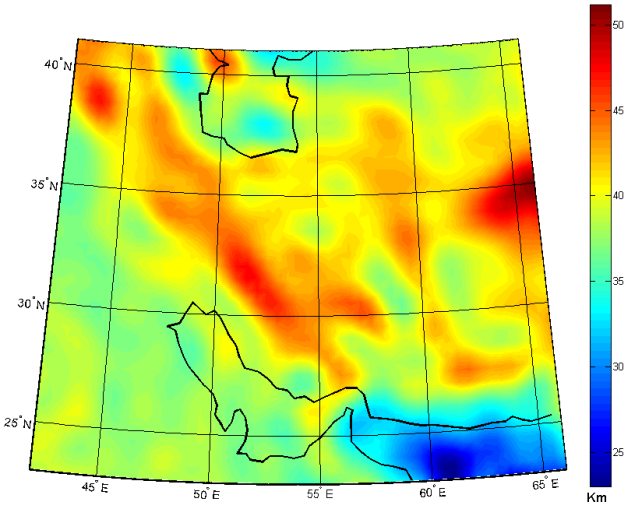

The estimated Moho depth

• Advanced Satellite Positioning

▫ An overview of precise point positioning

▫ RINEX data processing for positioning according to pseudorange and carrier phase observations by programming in MATLAB

▫ GPS data processing with GAMIT

▫ MATLAB programming for computation of the position, velocity and acceleration vectors of GPS satellites from precise ephemerides (in SP3 format) using polynomial interpolation, and moving average for precise orbit determination

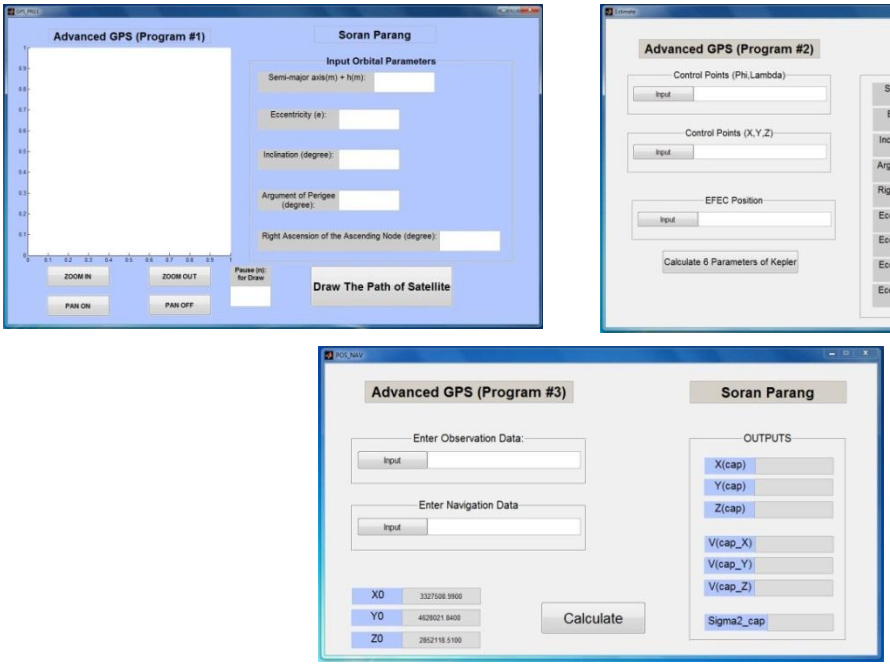

The MATLAB GUI programs, which I have written for this course project

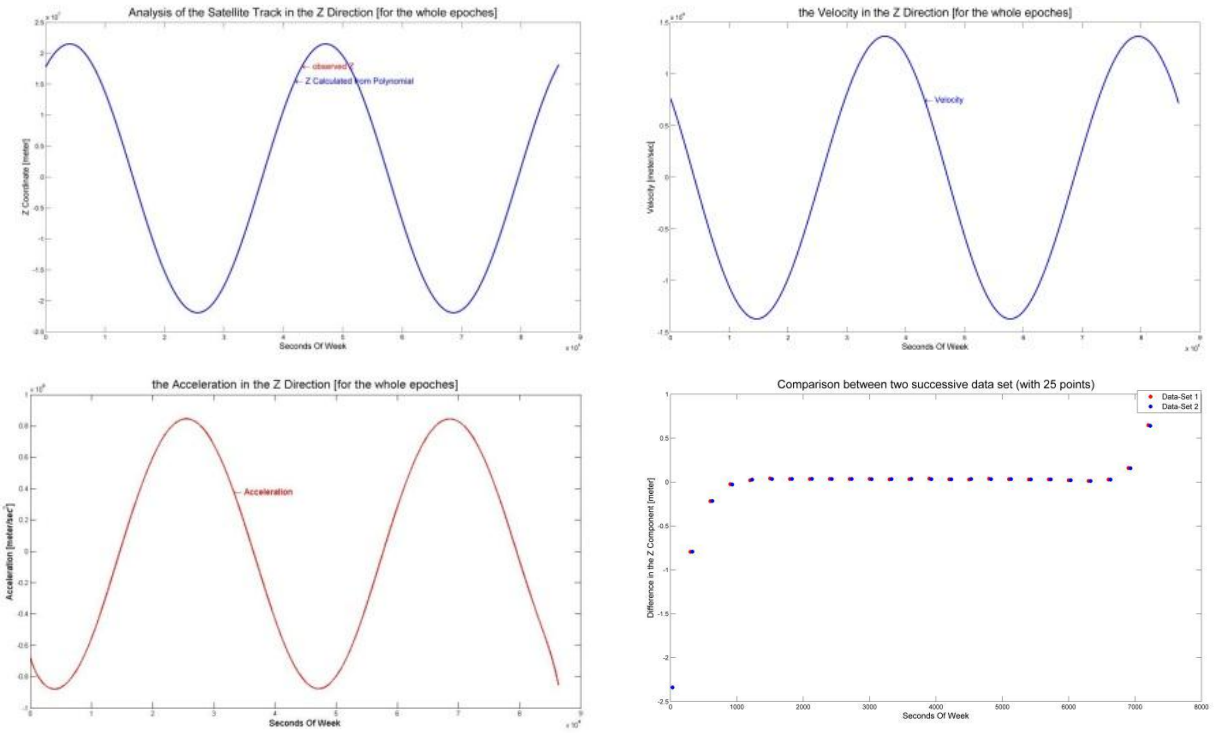

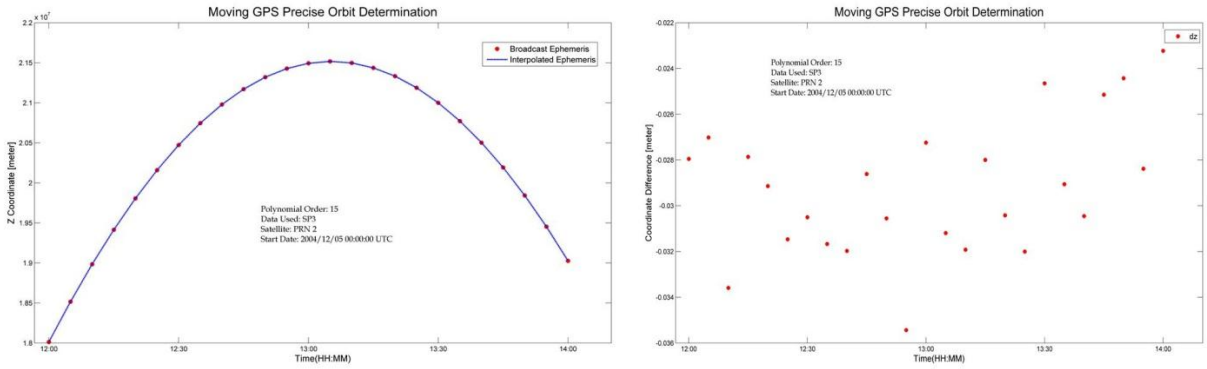

The results of polynomial interpolation of GPS satellite positions

- **Approximation Theory and Time Series Analysis**

  - **Geoid determination using least squares collocation and gravimetric observations**
  - **Image processing using wavelet transformation**
  - **Detection of cycle slip from GPS observations using wavelet transformation**

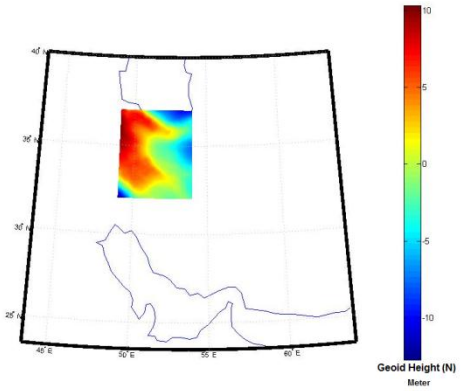

Geoid Height (N) obtained from least squares collocation

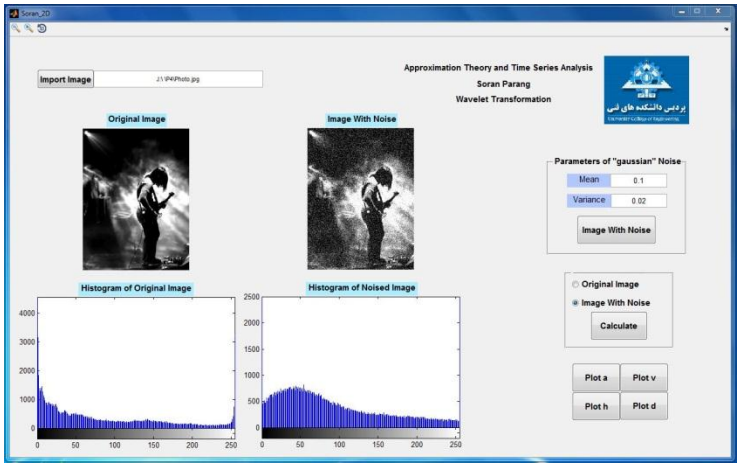

The MATLAB GUI program for image processing using wavelet transformation

- **Advanced Geodynamics**

  - **Strain analysis (Case study: Los Angeles basin)**
  - **Forward and Inverse modeling using Okada 85 model (Case study: 2003 Bam earthquake, Iran)**

- **Determination of Coseismic and Afterslip model using Okada 85 model (Case study: 1999 Izmit earthquake, Turkey)**
- **Calculating postseismic deformation and crustal layering effect using PSGRN code**
- **Research on slow and silent earthquakes**

Some MATLAB GUI programs, which I have written for this course project:

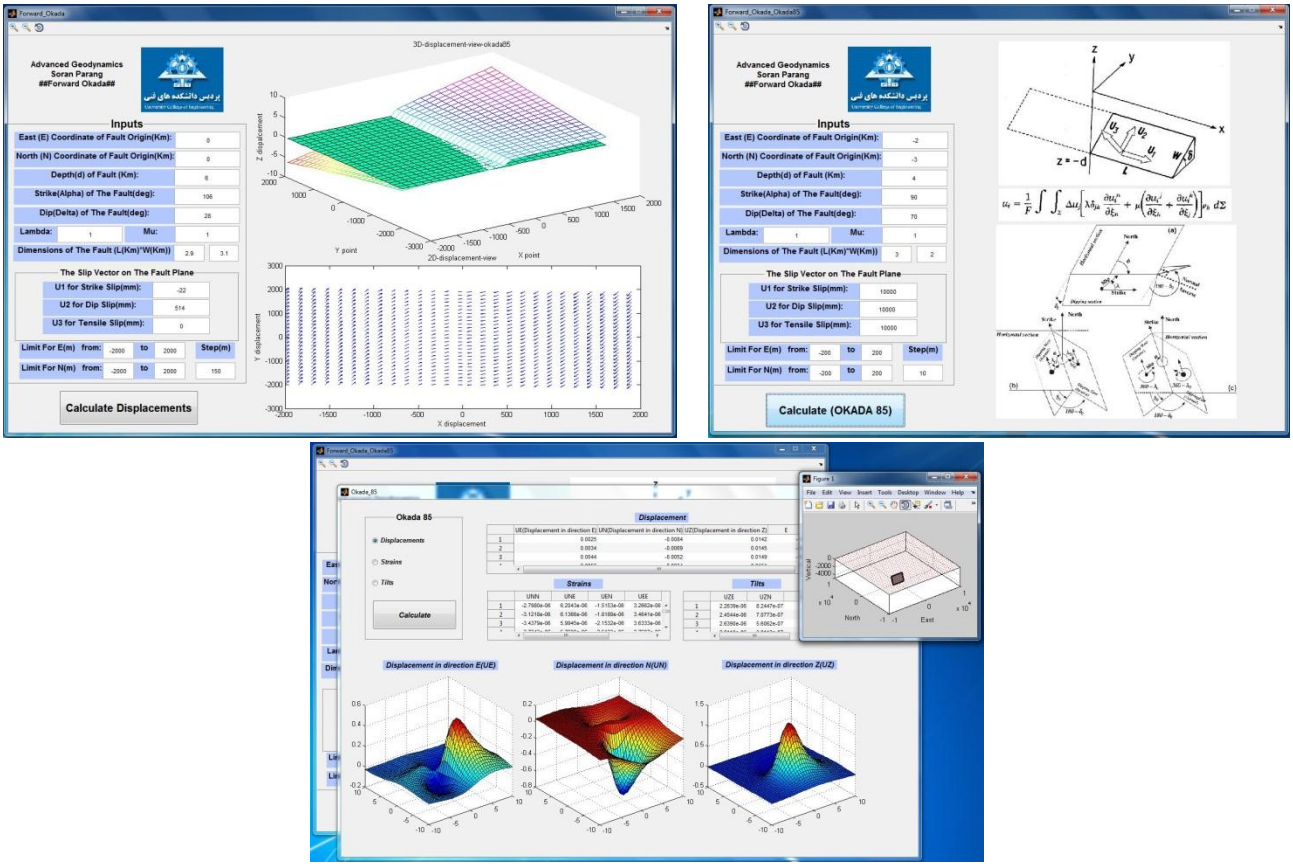

The MATLAB GUI programs for calculating the deformation due to a fault based on Okada 85 model

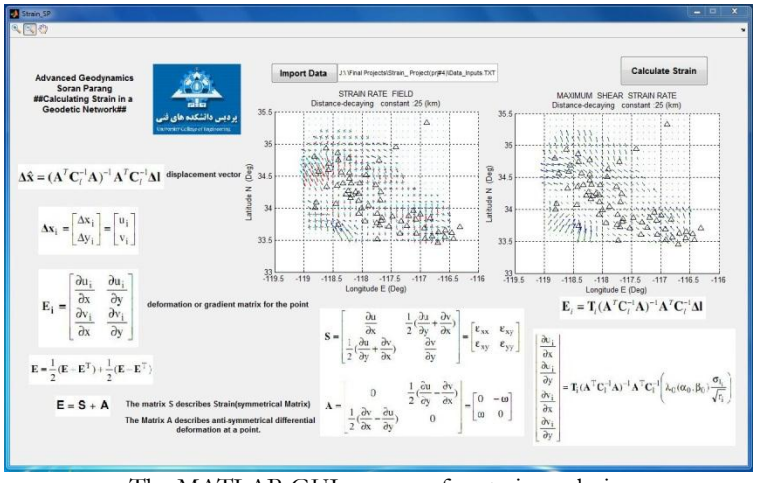

The MATLAB GUI program for strain analysis

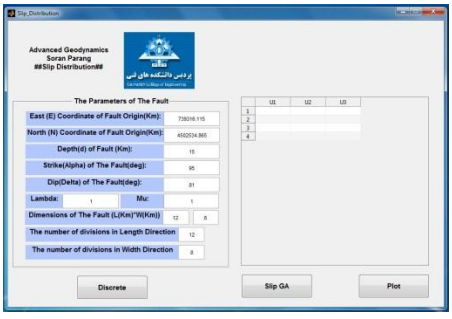

The MATLAB GUI program for determining slip distribution

• The Determination of the Fault Geometric Parameters by Solving Inverse Problem According to Okada Model & Genetic Algorithm, Case Study: Bam Earthquake in Iran

The existence of ruptures on the Earth's surface, known as faults, is a major factor in generating earthquakes. As a result, the identification of its geometry is highly significant for predicting natural disasters. There are several analytical models for faults, one of which is the Okada 85 model. Using an inversion problem defined by this model and displacement field estimated in the studied region, the geometric parameters of a fault considered as unknown parameters can be predicted. In this research, the displacement field, coseismic interferogram, derived from the BAM earthquake (occurred in December 26, 2003, southeastern Iran) was determined by ENVISAT ASAR radar images (3 SAR Images in descending orbit) and DInSAR technique. The estimated displacement field was considered as the observational field in the inversion problem formed by the Okada model and the unknown parameters, namely geometrical parameters of the fault, were calculated through the genetic algorithm and finally the slip distribution model was determined.

Estimating source geometry from geodetic data requires a forward model of how the crust responds to various kinds of deformation sources. The most common used crustal model is the homogeneous, isotropic, linear, elastic half-space proposed by Okada (1985). Accordingly, the displacement field $u_i(x_1, x_2, x_3)$ due to a dislocation $\Delta u_j (\xi_1, \xi_2, \xi_3)$ across a surface $\sum$ in an isotropic medium is:

$$u_i = \frac{1}{F}\iint_{\Sigma} \Delta u_j \left[\lambda \delta_{jk} \frac{\partial u_i^n}{\partial \xi_n} + \mu\left(\frac{\partial u_i^j}{\partial \xi_k} + \frac{\partial u_i^k}{\partial \xi_j}\right) v_k\right] d\Sigma$$

Where δ_{jk} is the Kronecker delta, λ and μ are Lame's coefficients (these parameters specify the elastic medium), v_k is the direction cosine of the normal to the surface element $d\Sigma$, and the summation convention applies. u_i^j is the ith component of the displacement at (x_1,x_2,x_3) due to the jth direction point force of magnitude F at (ξ_1, ξ_2, ξ_3). Consequently, through this model, a fault is represented by a rectangular dislocation, with uniform slip, embedded in a homogeneous, isotropic, elastic half-space. This dislocation is defined by nine model parameters that describe the geometry and the slip of the fault plane: longitude and latitude of a corner of the fault plane (E_0, N_0), length (L), width (W), strike (α), dip (δ) and depth (d_0) of the upper edge of the fault plane, and magnitude and rake of the slip vector (U_1,U_2). In spite of its limitations, the elastic half-space model is widely used primarily because of the simplicity of the expressions for the surface deformation caused by uniform, rectangular dislocations and point sources.

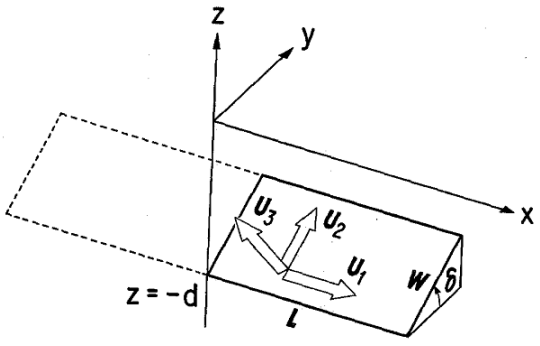

Geometry of the source model (Okada 1985)

Acquired answers from genetic algorithm

Width (km)	Length(km)	Depth (km)	Total Slip(m): $S = \sqrt{U_1^2 + U_2^2}$	Strike(deg)	Dip(deg)
8.84	12.78	6.85	2.42	177.8	88.6

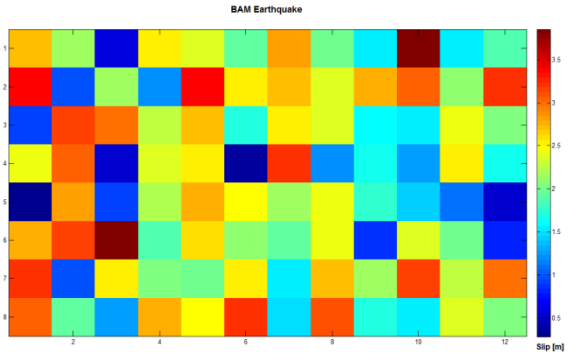

Slip distribution for the BAM earthquake from discretization and regularization

You can read more

• The Determination of a Fault Displacement Field According to Okada 85 Model and the Analysis of its Sensibility toward the Fault Geometric Parameters

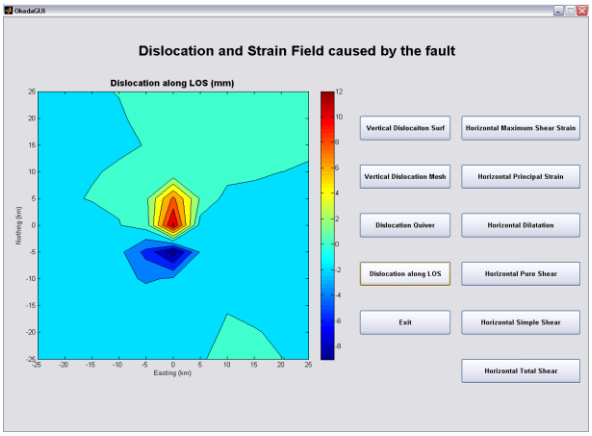

The program designed for this project

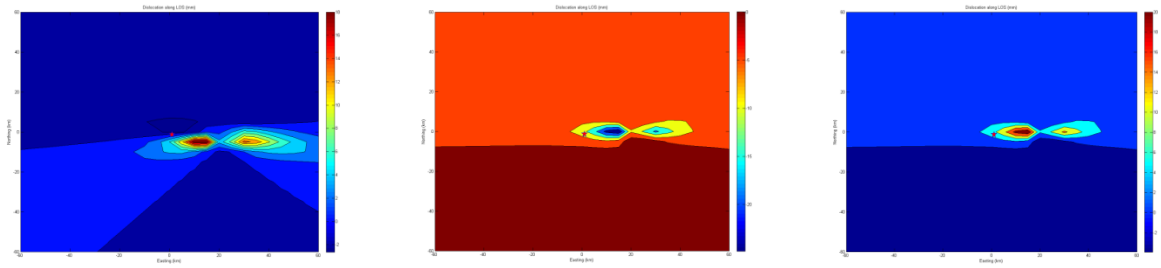

a **b** **c**

Displacement field along LOS for strike slip, thrust and normal faults. (a): strike-slip fault, (b): normal fault, (c): thrust fault

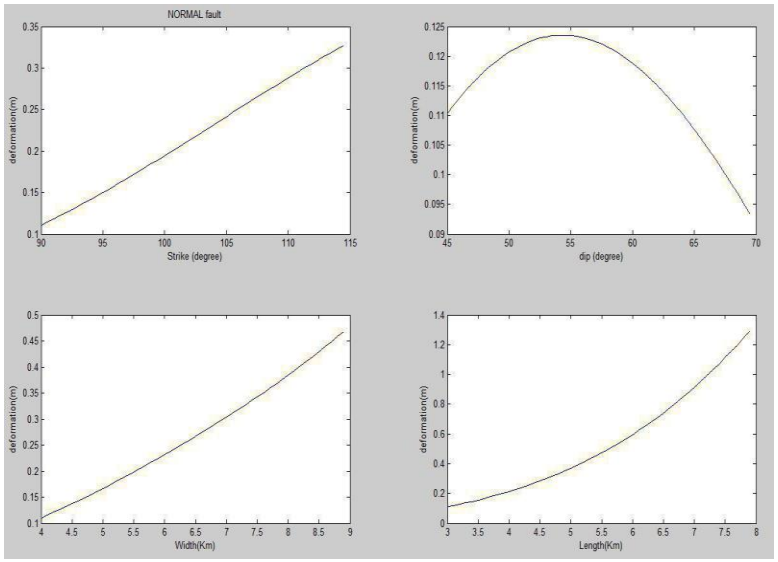

The sensitivity analysis of a normal fault relative to strike, dip, width, and length

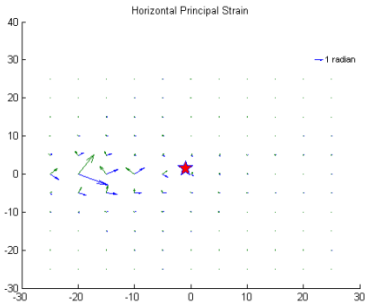

the principle strain field of a normal fault

You can read more

• Satellite Gravimetry

▫ MATLAB programming for determining the visibility and ground track of a satellite according to its orbital parameters

▫ Determining the keplerian elements and their standard deviations from position and velocity vectors

▫ Determining the dynamic orbit of a low earth orbiting satellite using numerical methods

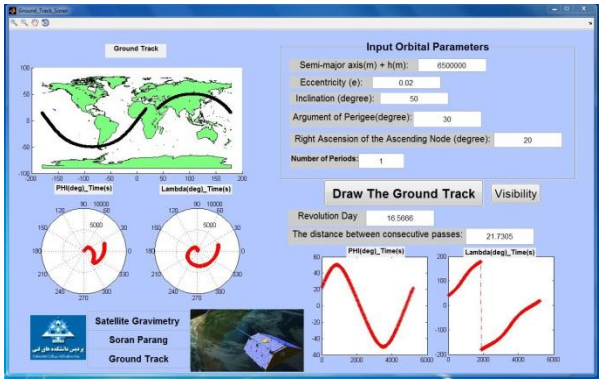

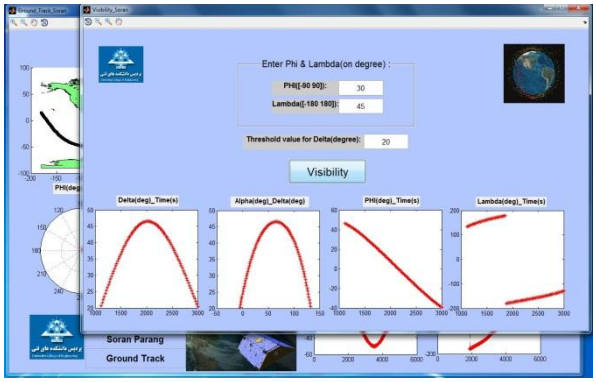

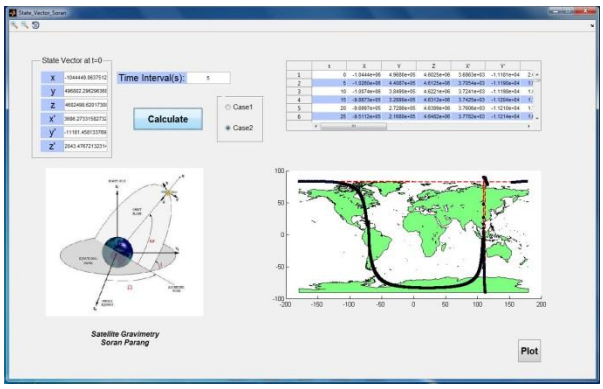

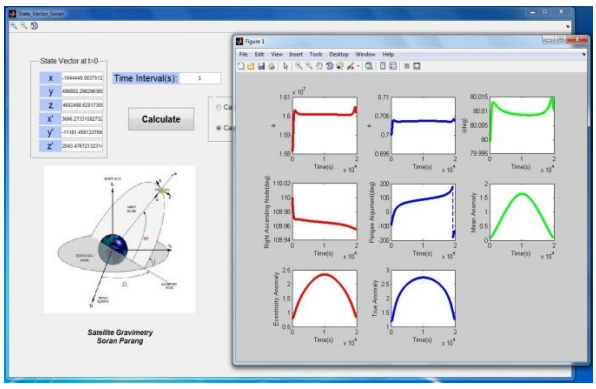

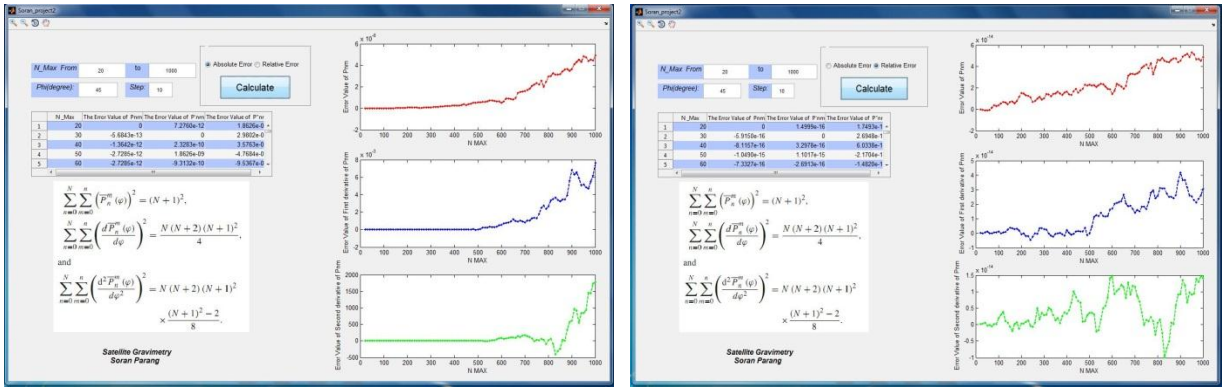

Some MATLAB GUI programs, which I have written for this course project

• Special Studies in Geometrical Geodesy

▫ Conversion of Single Look Complex (SLC) data from Level 1 products to Multi Look Intensity (MLI) images, the respectively performed processes: Radiometric Calibration; Multilooking; Speckle Filtering and Terrain Correction

▫ Determination of displacement field using InSAR technique and ENVISAT ASAR Images (Case studies: 2003 Bam and 2008 Qeshm earthquakes, Iran)

▫ Time series analysis via small baseline subset approach and DInSAR technique (Case Study: Land Subsidence in Mashhad plain, Iran)

▫ Surface displacement measurement using optical satellite imagery and COSI-Corr module in ENVI (Case Study: 2005 Kashmir earthquake)

▫ Research on 2D phase unwrapping

You can read more

The results of 2-pass differential interferometry method for the 2008 Qeshm earthquake:

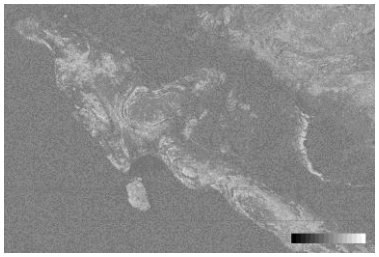
Coherence

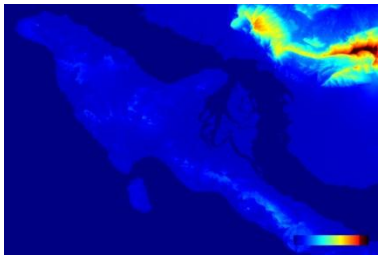
Comprefdem_height

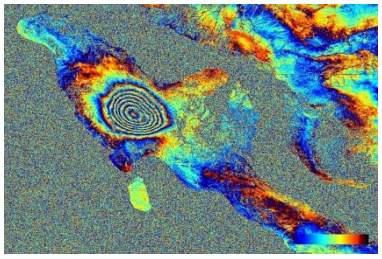
Interferogram_srd_pha

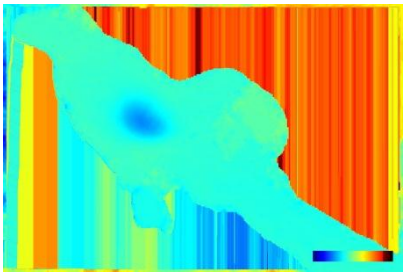
Unwrapped Interferogram

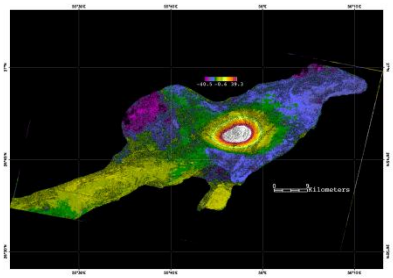
Displacement Field

The results of 2-pass differential interferometry method for the 2003 Bam earthquake:

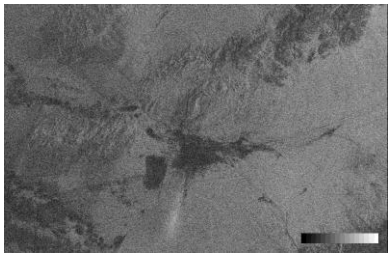

Coherence

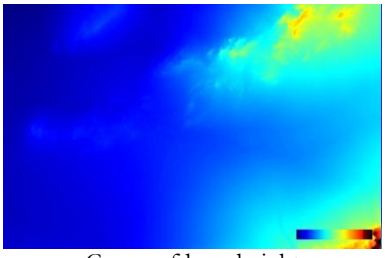

Comprefdem_height

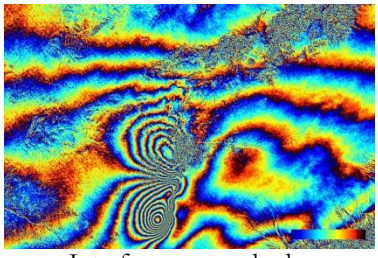

Interferogram_srd_pha

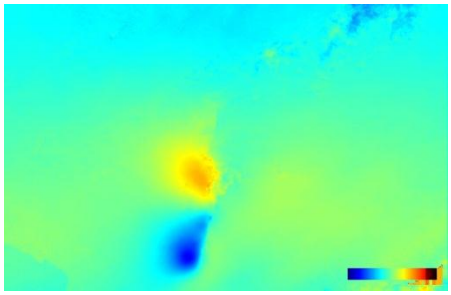

Unwrapped Interferogram

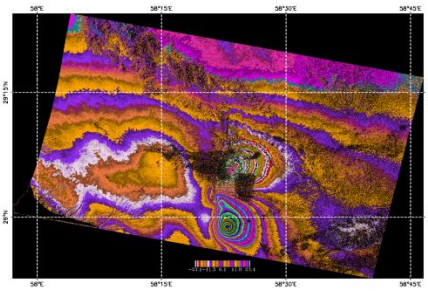

Displacement Field

The results of 3-pass differential interferometry method for the 2003 Bam earthquake:

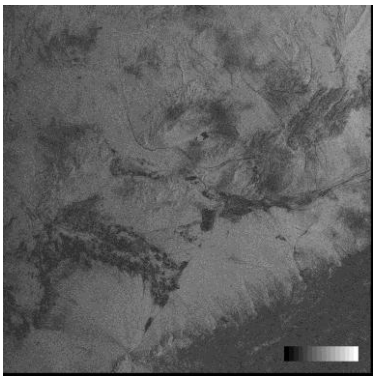

Coherence

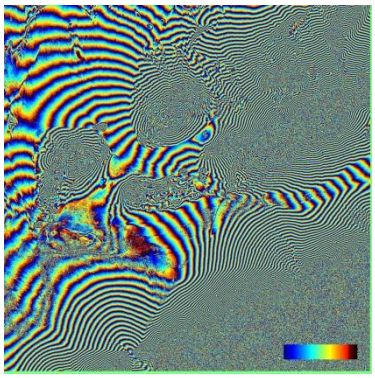

Interferogram_srp_pha

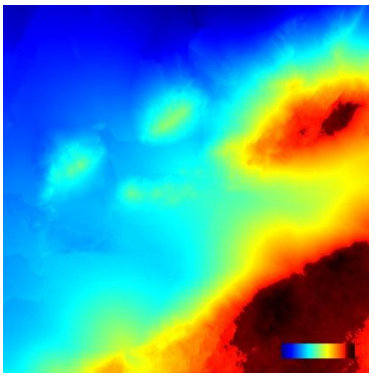

Unwrapped Interferogram

Topo Pair

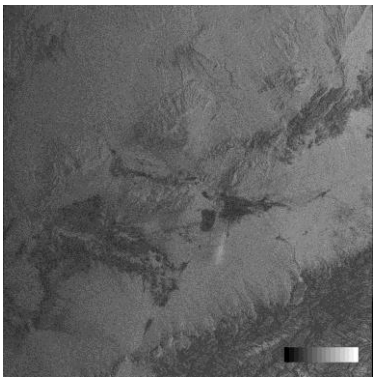

Coherence

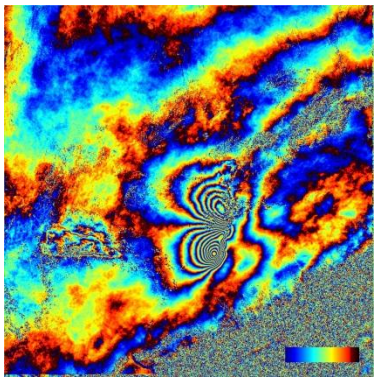

Interferogram_dinsar_pha

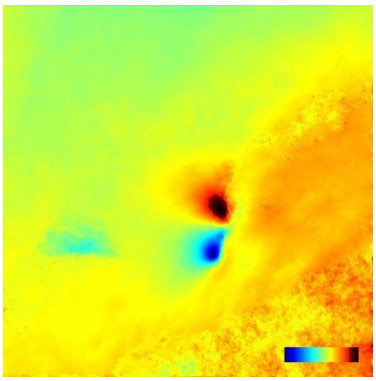

Unwrapped Interferogram

Defo Pair

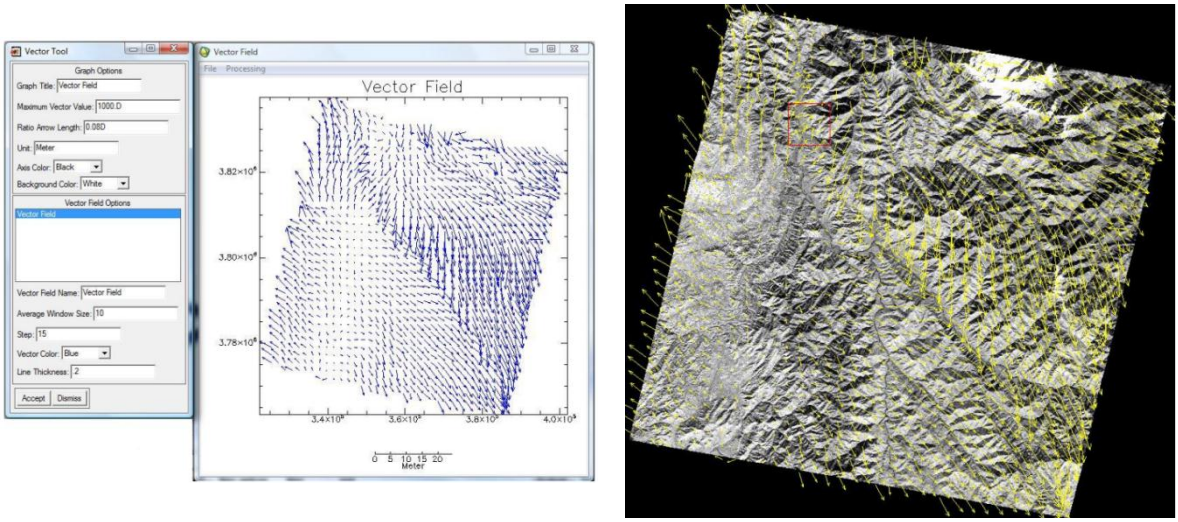

Surface displacement field produced by COSI-Corr for the 2005 Kashmir earthquake

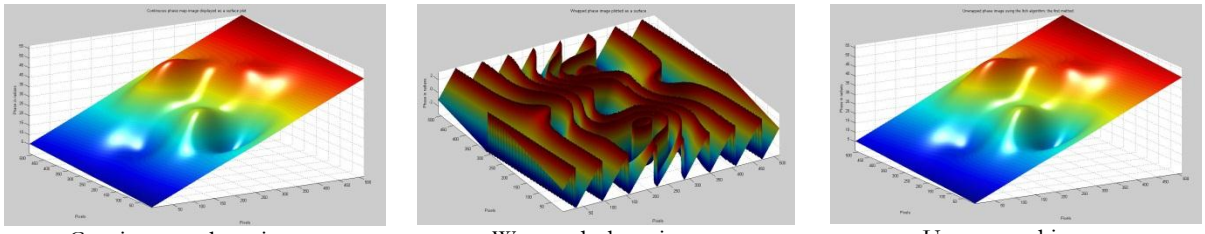

Continuous phase image | Wrapped phase image | Unwrapped image

2D Phase Unwrapping

• Advanced Physical Geodesy

▫ MATLAB programming for transforming spherical harmonic coefficients into ellipsoidal harmonic coefficients

▫ Calculating different gravity field functionals from the spherical harmonic models

▫ Comparison of geoid height derived from Geopotential Models with GPS leveling data in Iran

• A GIS-based Air Pollution Modeling in Tehran

The population growth, development of the mega cities and their impacts on urban traffic are the most important problems of the mega cities. Increased traffic volume and air pollution lead to population health problem. In this research, a prediction model has been proposed for air pollution prediction in 2004 using the data of 2002 and 2003 comparing the prediction results with the actual results of 2004. In addition, by using the method of local contribution to concentration in canyon streets, the concentration of both CO and NO at each month for six highways of Tehran and for each vehicle is calculated. The prediction model is a combination of CORINIER and Gualtieri-Tartaglia models. The proposal GIS-based model employs street geometry and vehicle numbers. Operation of CO and NO models Shows accuracy of 90% and 60% respectively. The results are appropriate for one year prediction of CO, whereas, for NO, it is not appropriate and the innovation in this paper is that the results of the previous modeling (Gualtieri-Tartaglia) results are valid for about one day, however, in this paper, by improving the model of Gualtieri-Tartaglia integrated with the CORINIER method, the model can be applied to estimate the air pollution within one year. The implemented data in this paper include the average monthly values of NO and CO in the second half-year of 2002 and whole years of 2003 and 2004. CO data used during 2005-2010 provided the similar results.

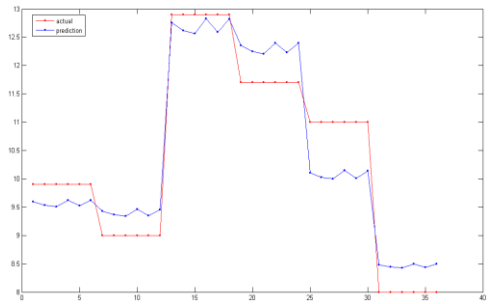

Estimation of 2002 with 2002 coefficients for CO, d = 97%

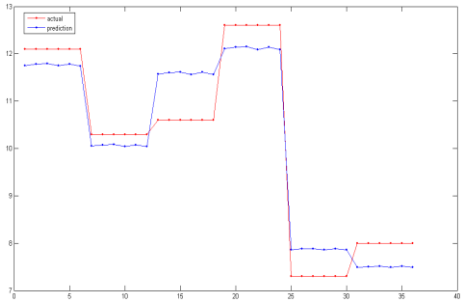

Estimation of 2003 with 2003 coefficients for CO, d =97%

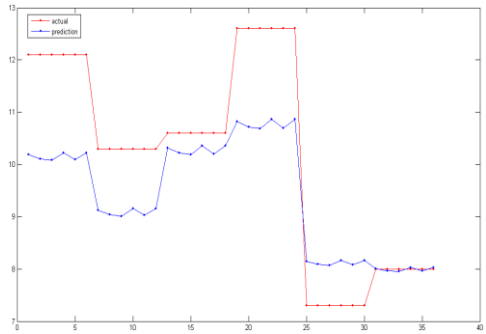

Prediction of CO 2004 with 2003 coefficients, d=90%

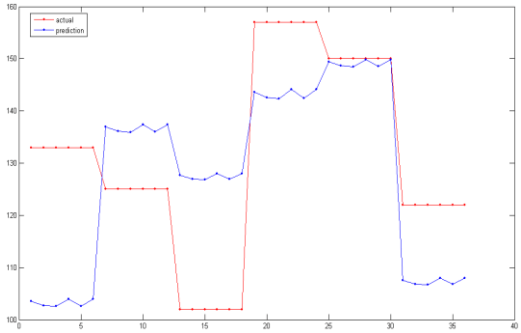

Prediction of NO 2004 with 2003 coefficients, d=65%

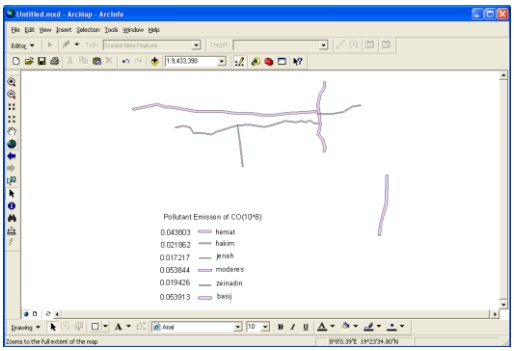

An example of pollutant emission mapping due to all traffic volumes in Tehran; Case study: CO for January 2004 emission rate

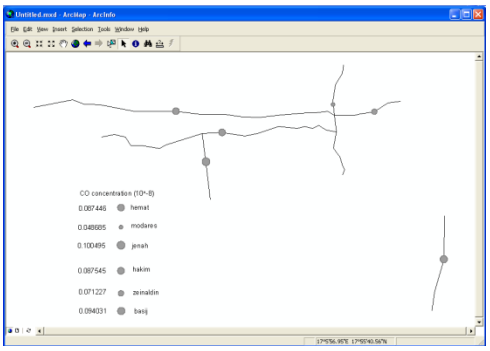

An example of pollutant dispersion mapping in Tehran; Case study concerning CO concentrations in January 2004

• Comparison of Seismic Moment Rates Obtained by Geophysical and Geological Methods in Structural Zones of Iran

Seismic moment as the released energy of earthquakes or the available energy in the faults is discussed as seismic moment rate based upon the time. This rate, which is functional in the determination of the seismicity of different regions, can be calculated according to different data and ways. In this research, the geological and geophysical methods have been used for calculating this parameter. Geological method uses the fault's parameters and geophysical method employs earthquake catalog. In this study, considering structural zones of Iran and density of earthquakes, seven regions for the calculation of moment rate have been chosen. As a result, the maximum value of moment rate acquired by geophysical method is related to the east of Iran (including Lut block) that is 3.7×10^{18} Nm/yr. In fact, high seismic moment rate in this region indicates the concentration of earthquakes in the east of Iran according to structural zones. Additionally, the maximum value of moment rate acquired by geological method is associated with the south-east part of Iran (Makran) that is 14.9×10^{18} Nm/yr, which shows the excessive activity of Makran fault. The ratio of two rates indicates that the earthquake catalog in the considered structural zones will estimate the number of earthquakes and the value of scalar moment less.

Results of seismic moment rate determination

Structural Units	Geophysical Moment Rate [10^{18} Nm/yr]	Geological Moment Rate [10^{18} Nm/yr]	Ratio of Geological Moment Rate to Geophysical Moment Rate
North West	0.9539	5.5804	5.8
North East (Kopeh Dagh)	2.1989	2.9285	1.3
Alborz	2.1380	6.7774	3.2
Zagros Fold & Thrust Belt	1.7737	6.5737	3.7
Central Domain	0.0283	3.5674	126
East (Lut Block)	3.7250	5.8526	1.6
South East (Makran)	0.3057	14.973	49

• Landslide Susceptibility Map using Bivariate Statistical Analysis, a Case Study in Bogota

Landslides occur in all regions of the world due to preparatory, triggering, sustaining and precondition (predisposing) factors. Researching for landslide hazard and risk has become a critical research for the international community over the last decade. In this research, the bivariate statistical method was utilized in order to create landslide susceptibility map based on quantitatively defined weight values. The main and relevant factors for producing susceptibility map are slope, land use and geology maps. After assigning specific weights for each class of maps, all weight maps were combined into a single map using certain combination rules.

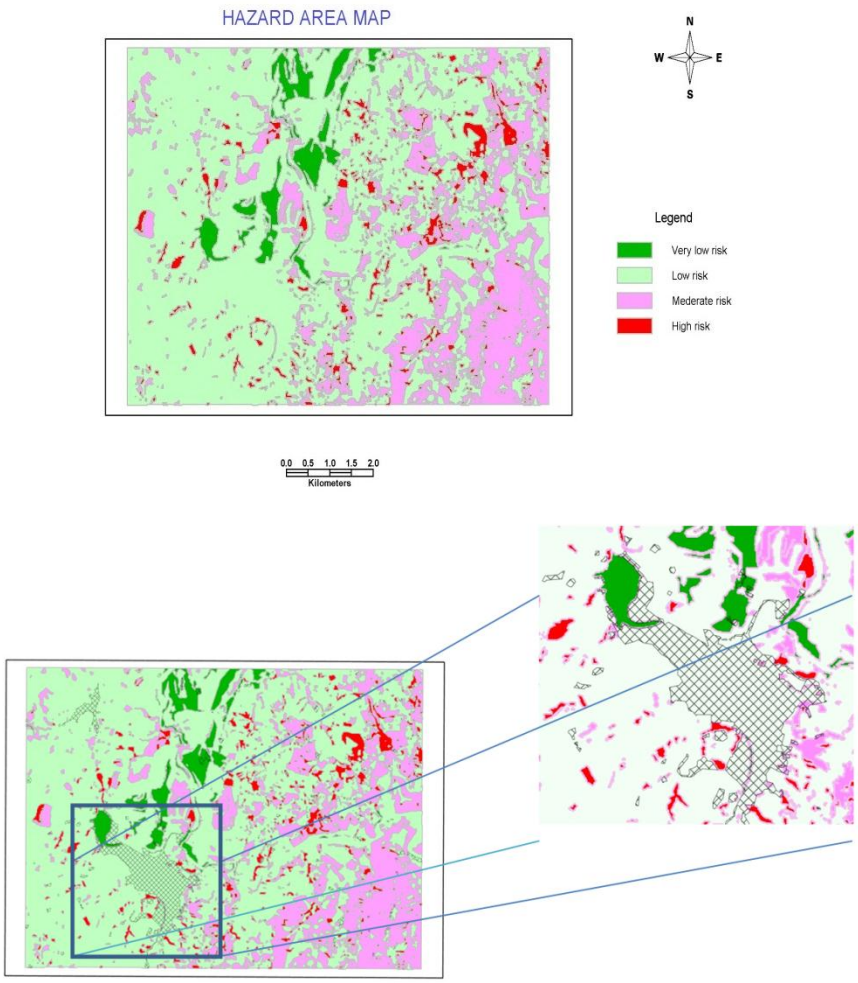

Hazard area map (the hatch area is urban)

You can read more

• **Image Processing**

Image Enhancement in the spatial and frequency domains, Image Segmentation

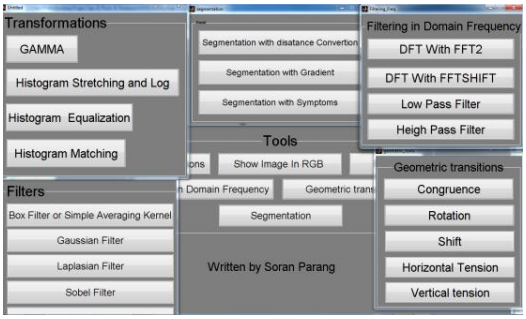

The MATLAB GUI package for image processing

• **Remote Sensing**

Classification, Geometric correction of multispectral images, Calculating NDVI and EVI

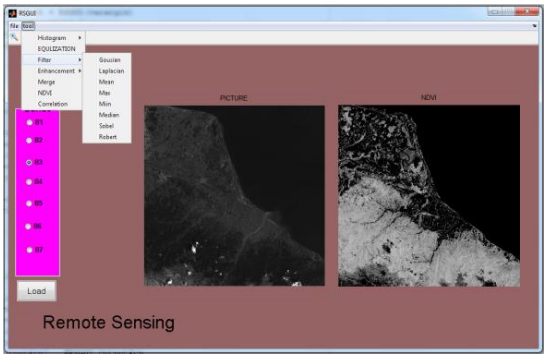

The MATLAB GUI program written for remote sensing

• **Photogrammetry**

Interior and exterior orientation, Intersection and resection, and bundle adjustment by programming and different types of software

The MATLAB GUI programs for photogrammetry

• **Microgeodesy**

Design, Pre-Analysis, Data processing and adjustment in various types of geodetic networks

• **GPS**

Processing and post processing of GPS data for positioning, Differential GPS, Adjustment of observations

• **Geodesy**

Inverse and direct problem, Datum conversion

• Hydrography

Determining Mean Sea Level (MSL), Chart Datum (CD), Mean High Water Neap & Spring (MHWN & MHWS), Mean Low Water Neap & Spring(MLWN & MLWS), Tide Predictions and Computations

• GIS

Finding optimal routes and site selection using Multi Criteria Decision Making Methods like AHP and ANP *You can read more*

• Hydrology

Estimating maximum discharge and determining basin boundaries

• Route Design

Analog, Digital

• Surveying

Producing topography map, Designing, Staking Out, Leveling, Volumes of land operations of primary road variant

• Subsurface Surveying

Tunnel